The orbital architecture and stability of the μ Arae planetary system

K. Goździewski ★

Institute of Astronomy, Faculty of Physics, Astronomy and Informatics, Nicolaus Copernicus University, Grudziądzka 5, PL-87-100 Toruń, Poland

ABSTRACT

We re-analyse the global orbital architecture and dynamical stability of the HD 160691 planetary system. We have updated the best-fitting elements and minimal masses of the planets based on literature precision radial velocity (RV) measurements, now spanning 15 yr. This is twice the RVs interval used for the first characterization of the system in 2006. It consists of a Saturn- and two Jupiter-mass planets in low-eccentric orbits resembling the Earth–Mars–Jupiter configuration in the Solar system, as well as the close-in warm Neptune with a mass of $\simeq 14$ Earth masses. Here, we constrain this early solution with the outermost period to be accurate to one month. The best-fitting Newtonian model is characterized by moderate eccentricities of the most massive planets below 0.1 with small uncertainties $\simeq 0.02$. It is close but meaningfully separated from the 2e:1b mean motion resonance of the Saturn–Jupiter-like pair, but may be close to weak three-body MMRs. The system appears rigorously stable over a wide region of parameter space covering uncertainties of several σ. The system stability is robust to a five-fold increase in the minimal masses, consistent with a wide range of inclinations, from $\simeq 20°$ to $90°$. This means that all planetary masses are safely below the brown dwarf mass limit. We found a weak statistical indication of the likely system inclination $I \simeq 20°–30°$. Given the well-constrained orbital solution, we also investigate the structure of hypothetical debris discs, which are analogues of the Main Belt and Kuiper Belt, and may naturally occur in this system.

Key words: methods: data analysis – methods: numerical – techniques: radial velocities – celestial mechanics – planets and satellites: dynamical evolution and stability – stars: individual: HD 160691.

1 INTRODUCTION

HD 160691 (μ Arae, GJ 691) is a bright ($V = 5.15$ mag) Sun-like, main-sequence G3IV-V dwarf monitored in a few long-term, precision radial velocity (RV) surveys. The Anglo-Australian Telescope team (AAT, UCLES spectrometer) discovered its Jupiter-mass companion HD 160691b in about of 630-d orbit (Butler et al. 2001), and Jones et al. (2002) found a linear trend in the RV data indicating a second, more distant planet. The star was also observed in the Geneva Planet Search program with CORALIE spectrometer. McCarthy et al. (2004) determined the orbital period of the outermost planet HD 160691c $\simeq 3000$ d and large eccentricity $e_c \sim 0.57$, however rendering the system unstable. The same year, Santos et al. (2004) detected $\simeq 14$ Earth-mass planet HD 160691d in $\simeq 9.6$ d orbit with HARPS spectrometer, achieving precision $\simeq 1$ m s^{-1}, actually below the RV variability (aka stellar jitter) induced by the Sun-like stars themselves. Furthermore, Butler et al. (2006) published 108 new observations of HD 160691, spanning about of 7.5 yr, made after AAT UCLES update, also approaching the measurement uncertainty below 1 m s^{-1} at the end of the observational window. Shortly, Pepe et al. (2007) published RVs from their HARPS followup, and announced the discovery of the fourth, Saturn-mass planet in the system. In parallel, Goździewski, Maciejewski & Migaszewski (2007) independently used genetic algorithms to re-analyse data in the Butler et al. (2006) catalogue, and they found a very similar

solution with small eccentricity orbits, also including the fourth planet with the orbital period $\simeq 307$ d. That planet 'hided' in the RV signal, because this period is approximately two times shorter as that of the firstly detected planet HD 160691b. Such a planet was unexpected in the paradigm of characterizing planets in order correlated with their RV variability. Goździewski et al. (2007) concluded that the four-planet system may be long-term stable in a wide range of the outermost period. However, it could not be constrained very well at that time, in $\simeq 3000$–5000 d range.

Since then, the star has continued to be RV-monitored. The HARPS measurements are now publicly available in the RV catalogue from archival spectra carefully reduced by Trifonov et al. (2020). Also, very recently Benedict et al. (2022) published additional 180 measurements from the UCLES spectrometer. The data altogether span 17.3 yr ($\simeq 6318$ d), between epochs JD 2450915.29 and JD 2457273.2878. Benedict et al. (2022) aimed to derive the new solution for the system based on combined RVs with *Hubble Space Telescope* (*HST*) astrometry. They investigated possible astrometric signals of the planets. They conclude that the residuals $\simeq 1$–2 mas to the canonical 5-parameter astrometric model contain marginal or no evidence for any of the planets in the HD 160691 system, making it possible only to constrain lower masses of the planets to 4– 7 m$_{\rm Jup}$ (i.e. 2–3 times larger than the minimal masses estimated with the RVs).

Furthermore, Benedict et al. (2022) report their updated Keplerian RV solution including the Saturn-mass planet as catastrophically unstable. They conclude that a notorious instability problem of the system remains unsolved, invoking Pepe et al. (2007), Laskar &

★ E-mail: k.Gozdziewski@umk.pl

Petit (2017), Agnew, Maddison & Horner (2018), and Timpe et al. (2013). This renewed our interest in the dynamics of HD 160691 system, given simultaneously our earlier, extensive investigations (Goździewski, Konacki & Maciejewski 2003, 2005), and the results in Goździewski et al. (2007). We came to quite the opposite conclusion that the four-planet architecture, and moderate eccentricity of all planets is *crucial* to maintain the long-term stability of the system. Actually, we found in Goździewski et al. (2007) that the 3-planet model involving only two outer Jovian planets is localized at the very border of dynamical stability, with planets in high-eccentricity orbits, and such a feature indicated that the adopted model was incomplete or incorrect.

Extending the RV time series puts the long-term monitored planetary systems deeper in the stability zone. A recent discussion of this heuristic effect can be found in Stalport et al. (2022). What is more, not only the RV data covers twice the time range in earlier work. The most accurate HARPS data recently been independently reprocessed using a new RV pipeline by Trifonov et al. (2020). They discovered and removed various systematic errors in a large sample of spectra. In some cases, they claim, the new RVs with improved accuracy can lead to orbital solutions different or more accurate from those found so far, including the hope of detecting additional planets. All of this gives us ample opportunity to test earlier predictions. Our goal is also to update the system's position in stability diagrams and statistics of multiple systems, studied for example by Timpe et al. (2013) and Laskar & Petit (2017).

In addition to explaining this *qualitative* discrepancy between the results in Benedict et al. (2022) and in Goździewski et al. (2007) the motivation for this work is to answer several open questions which have not been previously addressed in the literature.

Since the current RV data covers almost twice the observational window since 2006, we want to constrain the orbit of Jupiter's outermost planet. It was determined with a large uncertainty of 700 d reported in Pepe et al. (2007) and an even larger uncertainty of ±1300 d in Goździewski et al. (2007).

Also, it is known that a sufficiently long interval of RVs data makes it possible to detect gravitational interactions between the planets (e.g. Laughlin & Chambers 2001). Until now, the RVs of μ Arae have been modelled in terms of a Keplerian parametrization of the orbital elements, since the interactions of its planets were not measurable at the time. In this kinematic approach, the inclination of the system remains completely unbounded. However, the most accurate Newtonian model can break the mass-inclination degeneracy, or at least constrain the masses of the planets indirectly through the stability requirement.

Our goal is also to resolve the open question of whether the inner Saturn–Jupiter planet pair is involved in the 2e:1b MMR, or whether it is only close to this resonance. As far as this is concerned, the conclusions in both Pepe et al. (2007) and Goździewski et al. (2007) were uncertain, as both types (resonance or near-resonance) of solutions were possible. However, this is crucial for explaining the apparent excess of planet pairs near low-order resonances (e.g. Petrovich, Malhotra & Tremaine 2013; Marzari 2018, and references therein). The detailed characterization of multiple planetary systems, including their orbital resonances, is one of the fundamental problems from the point of view of the theory of planet formation and for explaining their observed orbital architectures.

If our early predictions in Goździewski et al. (2007) hold, and we find a dynamically stable orbital architecture for the planets, it may be possible to study the structure of debris discs in the system, particularly in the broad zone between 1.5 and 5.2 au, and beyond the outermost planet. According to the packed planetary systems (PPS) hypothesis (Barnes & Greenberg 2007, and references therein), smaller planets may exist in the system, but below the current RV detection level, approximately $1 \, \text{m s}^{-1}$, which correspond to the Earth's mass range.

Finally, the highly hierarchical configuration of the HD 160691 planets imposes numerical problems in studying the long-term stability of the system, either through direct numerical integrations or by using the fast indicator approach, which is preferred in this work. Recall that the system contains a warm Neptune in an orbit of 9.6 d, as well as a very distant companion in an orbit of 4000d, forcing a huge reduction in the discretization step size. To solve this problem, we propose a new numerical algorithm called REM (Panichi, Goździewski & Turchetti 2017), which we proved to be a close analogue of the Maximum Lyapunov Exponent (MLE). In this work, we compare the results of this fast indicator with the well-tested and widespread MEGNO (Goździewski et al. 2001; Cincotta, Giordano & Simó 2003). We show that despite simplicity of the algorithm, the REM indicator yields 1:1 dynamic maps compared to MEGNO and still outperforms the later variational algorithm in terms of CPU overhead.

We attempt to answer the questions posed above from the perspective of both updated RV time series and constraints provided with astrometric observations, as well as new statistical formulations of the RV model, dynamic and computational tools that have emerged over the time since the studies of Goździewski et al. (2007) and Pepe et al. (2007); we note that Benedict et al. (2022) also modelled the RV using the former, now somewhat 'outdated' approach.

Planets discovered in the μ Arae system are named in different ways. Here, we adopt three designations: the first one is based on the star name, as the central object and subsequent Roman letters ('b', 'c', 'd', and so on) attributed to the planetary companions in the chronological order of their discovery (Goździewski et al. 2007). The second method is to enlist the planets according to their distance from the star, with digits '1', '2', '3', and so on. Finally, we use the names attributed to the planets by the International Astronomical Union (2015) in the NameExoWorld campaign[1], among firstly discovered 19 extrasolar planetary systems. They were inspired by characters from the famous *Don Quixote* book by Miguel de Cervantes. So the μ Arae system is composed of the host star Cervantes (HD 160691), and planetary companions HD 160691d (Dulcinea, planet '1'), HD 160691e (Rocinante, planet '2'), HD 160691b (Quijote, planet '3'), and HD 160691c (Sancho, planet '4'), respectively.

The paper is structured as follows. After this Section 1, we describe data sources used for this study in Section 2. We discuss planet detection limits, based on the astrometric *HST* data and their analysis reported in Benedict et al. (2022), as well as our independent simulations of the astrometric signal. In Section 2.3, we briefly recall essential details on the RV modeling in terms of Keplerian and Newtonian parametrization of the initial conditions (ICs) for multiplanet configurations, and we point out factors omitted in the prior literature. We report on a comparison of the results based on these two RVs parametrizations. Section 3 is devoted to the long-term stability of the system. We aim to bound the inclination of the system with the RVs alone, based on the Newtonian model and statistical and dynamical constrains. Section 4 is devoted to numerical simulations that reveal the dynamical structure of hypothetical debris discs in the system as well as indicate possible localization of additional smaller planets. The work is summarized in Section 5.

---

[1] https://www.nameexoworlds.iau.org/
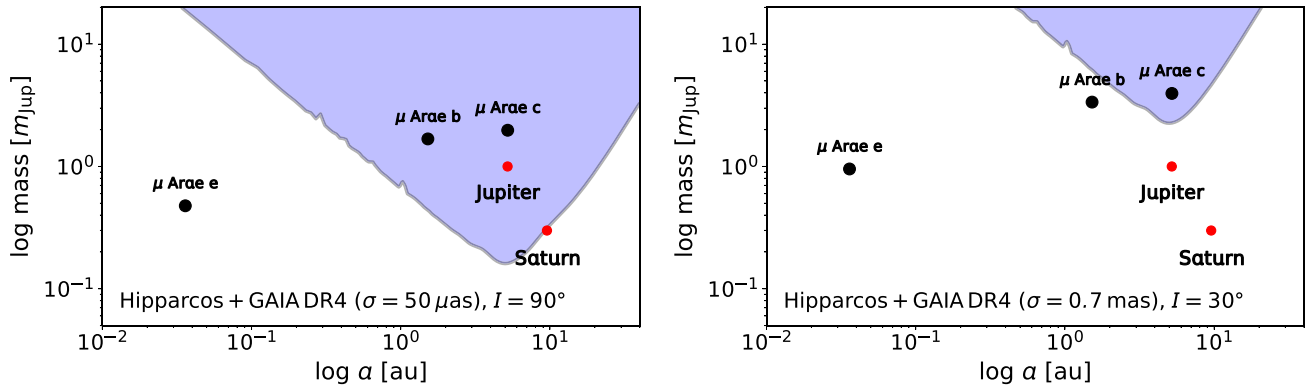
Figure 1. Astrometric detection limits in the mass–semimajor axis space for planets in circular, edge-on orbits simulated with the HTOF package (Brandt et al. 2021a), based on perturbed motion of the star due to the presence of planets. Objects in the blue-shaded region would be detected within the $\Delta\chi^2 > 30$ criterion when combining *Gaia* DR4 and *Hipparcos* IAD. (This criterion assumes $\Delta\chi^2 = 0$ for a free, inertial motion of the star). The left-hand panel is for edge-on orbits of the Saturn- and Jupiter-mass planets around μ Arae with the orbital elements listed in Table 2, Fit IIN. Jupiter and Saturn are marked for a reference. We assume extremely high-precision IAD in the anticipated *Gaia* DR4 catalogue, with the mean uncertainty of $50\,\mu$as. The right-hand panel is for the planet masses enlarged by the factor $1/\sin(30°)$, and artificial IAD accuracy of *Gaia* DR4 $\simeq 0.7$ mas, compatible with the declared *HST* FGS measurement precision reported in Benedict et al. (2022). There are planned 96 *Gaia* observations by the year of 2022, based on the *Gaia* Observation Forecast Tool (GOST).

2 THE REFLEX MOTION DATA FOR HD 160691

2.1 Astrometric observations

Benedict et al. (2022) observed HD 160691 with the *HST* Fine Guidance Sensor (FGS) between dates 2007.5 to 2010.4 (for about of 2 orbital periods of HD 160691b). They made a detailed reduction of the observations and reported the results. Overall, the accuracy of the astrometric measurements $\simeq 0.6$–0.7 mas, and the residuals to 5-elements canonical astrometric solution (no companions present) are estimated on the level of $\simeq 1$–2 mas. However, the periodogram analysis of these residuals, which might contain unmodelled factors and a signature of companions, does not show any significant period overlapping with the known orbital variability from the RV analysis. Unfortunately, also analysis of the proper mean motion based on the *HST* measurements by Benedict et al. (2022), and *Hipparcos* (van Leeuwen 2007) by Brandt (2021), respectively, relative to the estimates in the *Gaia* DR3 catalogue indicate that there is a marginal or lack of a measurable difference between the proper mean motion at the initial and the final epochs for 25 yr. That means there is difficult to detect a significant acceleration caused by the planetary companions, which was used, for instance, to astrometrically constrain the mass of the innermost planet HR 8799e in Brandt et al. (2021b).

Given the negative detection of any of the companions, Benedict et al. (2022) estimated the lower mass limits for HD 160691b,e,c as $(4.3, 7.0, 4.4)\,m_{\mathrm{Jup}}$, respectively, which could be consistent with a low inclination of the system below $I = 30°$. Moreover, they claim that inclinations in their sample of multiple-planetary systems are biased towards small values, $I \simeq 30°$ and less. As we show below, for HD 160691 this can be verified based of the RVs data alone.

Although the parallax of the system is large, $\Pi \simeq 64$ mas, the relatively small semimajor axes of the planets, compared to other astrometrically detected systems, translate to weak astrometric signals. To illustrate this effect, and to predict if the system may be characterized astrometrically by the ongoing *Gaia* mission, we simulated detection limits with the Intermediate Astrometric Data (IAD) from the *Hipparcos* and *Gaia* surveys. For this purpose, we used the HTOF package by Brandt et al. (2021a) which makes it possible to combine data from both missions, including IAD for

Gaia simulated with the help of *Gaia* Observation Forecast Tool (Gaia Collaboration 2021, GOST).

The results are illustrated in Fig. 1. The left-hand panel is for the detection limits for outer, massive planets assuming that the inclination $I = 90°$ and masses are minimal (a less favourable scenario). Then, assuming a superior mean accuracy of $\simeq 96$ *Gaia* measurements scheduled by the end of 2022, with the mean uncertainty $\sigma \simeq 50$ mas in the anticipated DR4 catalogue, and IADs from *Hipparcos*, we would easily detect the outermost pair of Jupiters. Note that the border of detection zone marks the astrometric detection criterion of $\Delta\chi^2 > 30$ by Perryman (Brandt et al. 2021a), when $\Delta\chi^2 = 0$ applies to the free motion of the star. However, the inner Saturn-mass planet remains deep below the detection limit (blue-shaded region).

The situation is dramatically worse, if a hypothetical data accuracy $\simeq 0.7$ mas is close to the *HST* FGS astrometry. Even if the system inclination is statistically most likely for $I = 60°$ or smaller, consistent with the inclination bias reported in Benedict et al. (2022), $I = 30°$, scaling the minimal masses by a factor of $\simeq 20$ per cent and $\simeq 100$ per cent, respectively, only the outermost planet could be barely detected with the astrometric time-series.

Unfortunately, these arguments and simulations leave little hope that a re-analysis of the available astrometric data may change the results and conclusions in Benedict et al. (2022) and Brandt (2021). Therefore we abandoned the *HST* astrometry from further analysis, and we focused on the RV observations only.

2.2 Radial Velocity data

We considered three slightly different sets of the RV measurements for μ Arae available in public archives and sources.

The RV data set $\mathcal{D}_1$ consists of 380 measurements spanning 6317.5 d. They are collected with three instruments: CORALIE ($\mathcal{D}_{\mathrm{CORALIE}}$), UCLES ($\mathcal{D}_{\mathrm{UCLES}}$), and HARPS ($\mathcal{D}_{\mathrm{HARPS1,2}}$). This set is literally the same as in Benedict et al. (2022), and we obtained it from the author (private communication). In densely sampled parts of the observational window, the data were binned if there was more than one measurement made during a night. The mean uncertainty is different for individual spectrometers, and varies between $\langle \sigma \rangle \sim$

1 m s^{-1} up to a several m s^{-1} for CORALIE. Moreover, Benedict et al. (2022) considered HARPS observations in two disjoint sets: from Pepe et al. (2007) and the second part of the time-series after that date from Trifonov et al. (2020). They attributed different RV offsets to these sets.

We also compiled a second data set $\mathcal{D}_2$. Trifonov et al. (2020) derived the RV velocities from spectra obtained prior – and post – the HARPS upgrade in May 2015, and corrected them for various systematics and instrumental effects. Since the available data for HD 160691 contains effectively only two post-upgrade measurements made in nights of 2015 June and July, we skipped these points from the orbital analysis. It would be difficult to account for two free parameters, σ_f and $V_0 \equiv V_{0,\,\mathrm{UCLES}}$, to be statistically determined with the RV subset comprising of only two datum. Moreover, because the post-upgrade HARPS epochs overlap with UCLES measurements, skipping them unlikely may change the model results. We also get rid of two free parameters. Similarly to Benedict et al. (2022), we also binned densely sampled measurements, but with a smaller interval of 0.1 d. Before doing that, we removed several points from the HARPS RV time series in Trifonov et al. (2020), with heavily outlying uncertainties of 10–24 m s^{-1}, given the mean uncertainty $\sigma_{\mathrm{HARPS}} \simeq 1$ m s^{-1}. The problematic measurements appear around JD 2453169 (2004 mid-June), when literally hundreds of spectra were taken overnight. Removing these points should not cause any problem, due to the dense sampling and binning. For the binned data in set $\mathcal{D}_2$, we adopted the uncertainties as the mean uncertainty in a given bin.

In this way, the data set $\mathcal{D}_2$ consists of the whole pre-upgrade HARPS measurements $\mathcal{D}_{\mathrm{HARPS}}$, as a homogeneous data set from Trifonov et al. (2020), and $\mathcal{D}_{\mathrm{CORALIE}}$ and $\mathcal{D}_{\mathrm{UCLES}}$ from Benedict et al. (2022). This set has 411 measurements and also spans 6317.5 d. To simplify presentation of the RV offsets, we subtracted the mean value of all RVs in a given subset from individual RVs in this subset.

Finally, in some experiments we considered data set $\mathcal{D}_3$ composed of 349 measurements from the pre-upgrade HARPS and $\mathcal{D}_{\mathrm{UCLES}}$ from Benedict et al. (2022). These RV time-series span the same time interval as $\mathcal{D}_2$ does. This data set $\mathcal{D}_3$ lacks the less accurate $\mathcal{D}_{\mathrm{CORALIE}}$ RVs.

2.3 Keplerian versus Newtonian Radial Velocities

The mathematical models for the RV velocities are well known. However, to keep the presentation self-consistent, and to cover some nuances, we will briefly recall the required material.

Since, following the prior literature, we expect that the μ Arae orbits may be quasi-circular, to get rid of weakly constrained longitudes of pericentre ϖ_i when eccentricities $e_i \sim 0$, we introduce Poincaré elements $\{x_i = e_i \cos \varpi_i, y_i = e_i \sin \varpi_i\}$, $i = 1, 2, 3, 4$. Also, the mean anomaly $\mathcal{M}$ at the selected initial epoch t_0 denoted as $\mathcal{M}_i \equiv \mathcal{M}_i(t_0)$ is defined through the III law of Kepler, but written for the Jacobian reference frame

$$P_i = 2\pi \sqrt{\frac{a_i^3}{k^2(m_0 + m_1 + \dots m_i)}}, \quad \mathcal{M}_i(t) = \mathcal{M}_i + \frac{2\pi}{P_i}(t - t_0),$$
(1)

where k is the Gauss constant, and P_i, a_i stand for the orbital period and semimajor-axis for each planet, respectively.

Regarding the Keplerian parametrization of the RV, we apply the well-known canonical formulae (Smart 1949) due to the presence of planets

$$C(t) \equiv V_r^{\mathrm{K}}(t) = \sum_i^{N_{\mathrm{pl}}} K_i \left[e_i \cos \omega_i + \cos(\nu_i + \omega_i) \right],$$
(2)

$$= \sum_i^{N_{\mathrm{pl}}} K_i \left[x_i + \left(x_i^2 + y_i^2\right)^{-1/2} (x_i \cos \nu_i - y_i \sin \nu_i) \right],$$
(3)

where $\omega \equiv \varpi$ for a coplanar system, $\nu \equiv \nu(t)$ denotes the true anomaly of a planet, N_{pl} is the number of planets in the system, and $\nu = \nu(P, e, \mathcal{M}(t))$. To characterize the orbit of the ith planet, we need to know five free orbital elements: $\boldsymbol{\theta}_i = [K_i, P_i, x_i \equiv e_i \cos \varpi_i, y_i \equiv e_i \sin \varpi_i, \mathcal{M}_i]$, where the RV semi-amplitude K_i depends on the minimal mass of the planet $m_i \sin I$, when the inclination $I = 90°$.

Let us note that we interpret the RV signal in terms of the geometric elements inferred in the Jacobian frame of reference. We follow here conclusions and discussion in Lee & Peale (2003), to properly express parameters of the Keplerian model through the N-body initial condition. We need that to investigate the long-term stability of the system with the numerical integrations. For relatively massive planets, the Jacobian (canonical) elements account for indirect interactions between the planets on Keplerian orbits to the first order in the masses (the ratio of planet masses to the star mass), see also Goździewski et al. (2012) for more details.

In order to derive the N-body initial condition from the fitted Keplerian elements $\boldsymbol{\theta}_i$, $i = 1, \dots, N_{\mathrm{pl}}$, we first determine the minimal masses $m_i \sin I \equiv m_i$ and semimajor axes a_i of the planets. The semi-amplitude K_i of the RV signal determines the relation

$$K_i \sqrt{1 - e_i^2} = a_i \left(\frac{2\pi}{P_i} \right) \frac{m_i}{(m_0 + m_1 + \dots + m_i)},$$

where the a_i constrained by the observationally derived orbital period P_i obeys equation (1), and m_0 stands for the star mass. Eliminating a_i, we obtain a cubic equation for the unknown masses, which may be subsequently solved for m_i, $i = 1, 2, \dots$, based on analytical formulae or with a simple Newton–Raphson scheme (a few iterations suffice to reach the machine accuracy). Then we transform the geometric elements to Cartesian coordinates and velocities with the standard two-body formulae, where the gravitational parameter for the ith planet is $\mu_i = k^2(m_0 + m_1 + \dots m_i)$.

To determine parameters of the orbital model explaining the RV time-series, we optimized a canonical form of the maximum-likelihood function $\mathcal{L}$ (Baluev 2009):

$$\ln \mathcal{L} = -\frac{1}{2} \sum_{i,t} \frac{(\mathrm{O\text{-}C})_{i,t}^2}{\sigma_{i,t}^2} - \frac{1}{2} \sum_{i,t} \ln \sigma_{i,t}^2 - \frac{1}{2} N_{\mathrm{RV}} \ln 2\pi,$$
(4)

where $(\mathrm{O} - \mathrm{C})_{i,t}$ is the (O–C) deviation of the observed t-th RV observation, with the uncertainty $\sigma_{i,t}^2 \to \sigma_{i,t}^2 + \sigma_f^2$, with σ_f parameter scaling the raw error $\sigma_{i,t}$ in quadrature, and N_{RV} is the total number of the RV observations. We assume that the uncertainties are Gaussian.

The error floor factors σ_f^2 are different for each telescope, as they may involve not only the intrinsic, chromospheric RV stellar variability (stellar jitter), but also instrumental uncertainties inherent to each telescope and the RV pipeline. The RV model also involves individual offsets of the zero-level RV for each instrument. Distinguishing between these two parameters is important even for the same spectrometer and different setups of its work. For instance, the upgrade of HARPS optical fibres around the middle of 2015 changed the instrumental profile and thus the RV offset between the pre- and post-upgrade RVs. To complicate things even more, the RV offset

may be not the same for all stars and may even depend on the stellar spectral type (Trifonov et al. 2020).

Therefore fitting the jitter uncertainties as free parameters of the model is crucial to obtain adequate statistical representation of the RV data. We may note here, that in the past, these parameters have been fixed based on the averaged values for chromospherically quiet stars of a given spectral type. That recently outdated (and somewhat incorrect) approach was used by Goździewski et al. (2007) and Pepe et al. (2007); Benedict et al. (2022) tuned the RV uncertainties to obtain $\chi_\nu^2 \simeq 1$.

Usually, the Keplerian model determines sufficiently accurately the N-body, exact RVs. However, for systems with large-mass planets, this equivalence may be questionable, especially if the interval of the RV time series becomes long. Then we have to introduce the self-consistent model that requires solving the Newtonian equations of motion. The RV due to the planets is the velocity component of the star along the z-axis w.r.t. the barycentre of the Solar system

$$C(t) \equiv V_r^{\rm N}(t) = -\frac{1}{m_0} \sum_{i=1}^{N_{\rm pl}} m_i \dot{z}_i(t), \qquad (5)$$

which is parametrized through planet masses and the osculating orbital elements $\boldsymbol{\theta}_i = [m_i, a_i, x_i, y_i, \mathcal{M}_i]$ for each planet in the system. Here, as the osculating epoch we select the epoch of the first observation in the time series. In some experiments, we also selected the osculating epoch in the middle of the data window.

Expressions for the RVs, equations (2) and (5) have to be accompanied with the instrumental zero-level offsets $V_{0,j}$, $j = 1, \ldots, M$ that makes it possible to compute $(O - C)(t)$ in equation (4). For $N_{\rm pl}$-planets forming a coplanar system observed with M instruments, we have therefore $p = 5N + 2M$ free parameters to be fitted to 1D time series of the RV observations.

The definition in equation (4) is constructed so the best-fitting models should yield $\chi_\nu^2 = \chi^2/(N_{\rm RV} - p) \sim 1$, and χ_ν^2 cannot be used to compare the models quality. Instead, Baluev (2009) proposed to use:

$$\ln L = -\ln \mathcal{L}/N_{\rm RV} - \ln(2e\pi)/2,$$

where L is expressed in ms^{-1}. This statistics is suitable to assess the relative quality of fits, since $L \sim \langle\sigma\rangle$ measures a scatter of measurements around the best-fitting models, similar to the common RMS – smaller L means better fit.

In order to localize the best-fitting solutions in the multidimensional parameter space, we explore it with evolutionary algorithms (GEA from hereafter, Charbonneau 1995; Ruciński, Izzo & Biscani 2010). We then perform the MCMC analysis in the neighbourhood of selected solutions using an affine invariant ensemble sampler (Goodman & Weare 2010) encompassed in a great `emcee` package (Foreman-Mackey et al. 2013). The computations were performed in multi-CPU environment, making it possible to evaluate 128 000–256 000 (or more) of 144–384 `emcee` 'walkers' from a small-radius ball around a solution found with the GEA.

We select all priors as flat (or uniform, improper) by sufficiently broad ranges on the model parameters, e.g. $P_i \in [1, 10\,000]$ d, x_i, $y_i \in [-0.25, 0.25]$, $m_i \in [0.1, 14]$ $m_{\rm Jup}$, $(i = 1, 2, 3, 4)$, the error floors (jitters) $\sigma_{f,j} > 0$ m s^{-1}, $j = 1, \ldots, M$. In a few experiments with the N-body model, we also tested Gaussian priors for the (x_1, y_1) elements of the innermost planet, with the mean equal to zero and variances $\sigma_{x,y} = 0.05, 0.075, 0.1$, respectively. In this case, however, the results of sampling did not substantially change, compared to the flat priors.

2.4 The best-fitting orbital configurations

We first performed an extensive search for the best-fitting solutions using GEA, and we collected $\simeq 10^3$ solutions for the data sets and model variants. We found that the best-fitting Keplerian and Newtonian models with $L \simeq 3.2$ m s^{-1} (RMS $\simeq 3.4$ m s^{-1}) have well-determined extrema of $\ln \mathcal{L}$ for orbital periods P_i of roughly 9.64, 308, 645, and 4030 d, respectively. Also, all osculating eccentricities are limited to moderate values, roughly in the range of 0.02–0.1.

The resultig best-fitting parameters for data sets $\mathcal{D}_1$ and $\mathcal{D}_2$ are given in Tables 1 and 2. The best-fitting Keplerian model Fit IIK in Table 2 is illustrated in Fig. 2, left-hand panel. Using this solution as an example, we checked the consistency of the Keplerian and Newtonian parametrization. We transformed Fit IIK as osculating elements for the epoch of the first observation t_0 =JD 2450915.29 in the UCLES data, as described in Section 2.3. We then computed the Newtonian RV signal through of numerical integration of the N-body equations of motion for the entire four-planet system with the IAS15 integrator (Rein & Spiegel 2015). It turns out that the difference $\Delta \rm{RV}(t) = V_r^{\rm N}(t) - V_r^{\rm K}(t)$ increases in an oscillatory manner, reaching about ± 10 m s^{-1}, which exceeds more than twice the RV signal from the innermost planet (red curve in the residuals diagram in Fig. 2).

To verify this effect globally in the parameter space, we performed the MCMC sampling with both the Keplerian and Newtonian RV models. The final results for data set $\mathcal{D}_2$ are illustrated in Fig. 3. (We skip presentation of the results for $\mathcal{D}_1$, since they are very similar). This figure shows 1D and 2D projections of the posterior probability distribution for selected Keplerian (top row) and Newtonian (bottom row) orbital elements obtained for the innermost (left column) and outermost (right column) planet, respectively. The posterior has well defined extrema along all dimensions. We did not notice significant correlations between the displayed parameters, except for x, y, and $\mathcal{M}$.

The quality of the best-fitting configurations, in terms of RMS $\simeq 3.4$ m s^{-1}, is also almost the same. Surprisingly, the posterior distributions are not only very similar to each other, especially if we compare the 2D shape distributions for x, y, and $\mathcal{M}$, but also the eccentricities and orbital angles closely overlap, e.g. the best-fitting $\mathcal{M}_4$ anomaly differs by only $2^{\rm o}$ in these models.

How to interpret this apparent paradox, given the relatively large masses of Jupiter-like companions and their significant, mutual interactions over the observing interval, illustrated in Fig. 2? A direct comparison of the RV signals may be biased because the accuracy of the formal two-body Keplerian element transformation to Cartesian coordinates is limited to the first order in masses (e.g. Goździewski et al. 2012). However, the representation of the Keplerian initial condition for the N-body problem may better fit the data if it is tuned within the parameter uncertainties. Therefore, given well bounded orbital elements, the MCMC sampling reveals globally similar posteriors for both models.

We also see the posteriors for the near 2e:1b MMR pair of the Saturn–Jupiter-mass planets exhibiting some significant differences (see on-line Supplementary Material, Fig. S1). This can be explained by their relatively shorter periods, covering $\simeq 20$ and $\simeq 10$ times the observational window, respectively, and the 2e:1b MMR proximity, which strengthens the mutual gravitational interactions.

The MCMC experiment implies that, keeping in mind the limitation for representing individual ICs, we can still use Keplerian MCMC sampling to efficiently explore the parameter space, in terms of the posterior distribution, especially for highly hierarchical configurations with large period ratio. Note that $P_4/P_1 \simeq 400$ for

Table 1. Best-fitting parameters of the μ Arae (Cervantes) system for the Keplerian (Fit IK) and Newtonian (Fits IN) parametrization, data set $\mathcal{D}_1$. The osculating epoch is the date of the first observation in the UCLES data set. The system is coplanar with the inclination $I = 90°$ and nodal longitudes $\Omega = 0°$. The stellar mass is $1.13\,\mathrm{m}_\odot$ (Bonfanti et al. 2015) as used by Benedict et al. (2022), and close to $1.10 \pm 0.02\,\mathrm{m}_\odot$ in Soriano & Vauclair (2010). The RV offsets are computed w.r.t. the mean RV in each individual data set. Uncertainties are estimated around the median values μ, i.e. $[\mu - \sigma, \mu + \sigma]$ as the 16th and 86th percentile of the samples. Numerical values for Fit IN selected from the MCMC samples with low RMS are quoted to the 7th digit after the dot, to make it possible to reproduce the dynamical maps and direct numerical integrations. The mean longitude $\lambda = \varpi + \mathcal{M}$ at the epoch was computed from the MCMC samples.

Planet	HD 160691d (Dulcinea, 1)	HD 160691e (Rocinante, 2)	HD 160691b (Quijote, 3)	HD 160691c (Sancho, 4)
	Fit IK (Keplerian model of the RV, data set $\mathcal{D}_1$, RMS = $3.4\,\mathrm{m\,s^{-1}}$)			
$K\,(\mathrm{m\,s^{-1}})$	2.95 ± 0.19	13.22 ± 0.34	36.47 ± 0.22	23.17 ± 0.33
P (d)	9.638 ± 0.001	308.75 ± 0.29	645.00 ± 0.36	4060 ± 27
$e\cos\varpi$	-0.104 ± 0.063	-0.093 ± 0.014	0.058 ± 0.011	0.022 ± 0.012
$e\sin\varpi$	-0.059 ± 0.063	-0.014 ± 0.017	0.023 ± 0.008	0.032 ± 0.013
e	0.137 ± 0.056	0.096 ± 0.014	0.063 ± 0.010	0.040 ± 0.013
ϖ (deg)	210 ± 32	189 ± 10	$21.6 \pm (9.4,8.2)$	55.9 ± 17.5
$\mathcal{M}$ (deg)	223.3 ± 32	66.7 ± 10.5	$272.5 \pm (8.3,9.4)$	185.9 ± 17.2
λ (deg)	73.3 ± 10.5	255.4 ± 3.9	294.0 ± 1.0	241.9 ± 2.2
$V_0\,(\mathrm{m\,s^{-1}})$	CORALIE: 13.04 ± 0.42, UCLES: -7.80 ± 1.20, HARPS$_1$: 1.0 ± 0.3, HARPS$_2$: -4.20 ± 0.32			
$\sigma_f\,(\mathrm{m\,s^{-1}})$	CORALIE: 1.30 ± 0.21, UCLES: 6.1 ± 1.1, HARPS$_1$: 0.62 ± 0.46, HARPS$_2$: 1.67 ± 0.40			
	Fit IN (Newtonian model of the RV, data set $\mathcal{D}_1$, RMS = $3.4\,\mathrm{m\,s^{-1}}$)			
$m\sin I\,(m_{\mathrm{Jup}})$	0.033 ± 0.002	0.477 ± 0.012	1.680 ± 0.010	1.978 ± 0.028
	0.0333733	0.4805150	1.6894371	1.9415698
a (au)	$0.092319 \pm 6 \times 10^{-6}$	0.9376 ± 0.0015	1.521 ± 0.001	5.243 ± 0.023
	0.0923201	0.9358533	1.5204938	5.2228363
$e\cos\varpi$	-0.086 ± 0.067	-0.060 ± 0.014	0.057 ± 0.012	0.018 ± 0.012
$e\sin\varpi$	-0.063 ± 0.067	-0.031 ± 0.015	0.016 ± 0.008	0.026 ± 0.012
e	0.127 ± 0.057	0.069 ± 0.014	0.060 ± 0.011	0.034 ± 0.012
	0.0093112	0.0729955	0.0563256	0.0378130
ϖ (deg)	$215 \pm (36,38)$	$207.5 \pm (11.4,11.9)$	$16.4 \pm (10.3,8.2)$	56.4 ± 21.0
	52.8721947	217.8362502	19.7788422	52.2928770
$\mathcal{M}$ (deg)	$218 \pm (34,38)$	53 ± 14	$278 \pm (9,10)$	$187 \pm (21,20)$
	25.8318188	36.6741123	272.3695792	187.6140820
λ (deg)	76.9 ± 10.7	260.0 ± 4.0	293.3 ± 1.1	243.1 ± 2.1
$V_0\,(\mathrm{m\,s^{-1}})$	CORALIE: 13.10 ± 0.43, UCLES: -7.74 ± 1.14, HARPS$_1$: 1.10 ± 0.30, HARPS$_2$: -3.94 ± 0.32			
$\sigma_f\,(\mathrm{m\,s^{-1}})$	CORALIE: 1.23 ± 0.20, UCLES: $5.88 \pm (1.07,0.93)$, HARPS$_1$: 0.45 ± 0.40, HARPS$_2$: 1.51 ± 0.36			

HD 160691. However, direct parametrization in terms of the *N*-body dynamics is obviously more accurate approach to explain the RV variability when considering individual (local) best-fitting models.

To justify the above explanation, we compared the outcomes of the Keplerian and Newtonian fits for data set $\mathcal{D}_2$ in Table 2, and the results are illustrated in the (O–C) diagram in the right panel in Fig. 2. This time, the difference between the signals plotted as a red curve in the residuals diagram has much less variability, with the largest differences $\simeq 5\,\mathrm{m\,s^{-1}}$ appearing for epochs without data.

As noted above, an important feature of the posterior distributions is well bounded parameters for all planets. In particular, the semimajor axes of the middle pair, near 2e:1b-MMR (Rocinante–Quijote) are constrained to $\simeq 0.0015$–0.002 au, and for the outermost Sancho planet to just $\simeq 0.02$ au, i.e. its orbital period may be determined with the uncertainty of one month (25–50 times better than with the data in 2006). That seems to be quite surprising, since the observational window covers only about 1.5 times the period of this companion. Similarly, the Poincaré elements ($x_i = e_i\cos\varpi_i$, $y_i = e_i\sin\varpi_i$) of the Saturn- and Jovian planets may be determined to ± 0.01, with uncertainties of the arguments of pericentre and the mean anomalies at the osculating epoch t_0 on the level of $\pm 15°$. This translates to the mean longitude at the epoch λ_i that may be determined to $\simeq 4°$. The eccentricities in the Keplerian and Newtonian parametrizations

(Tables 1–2) are at the 0.05 level with small uncertainties, as we will show below, may be crucial for maintaining the long-term stability of the system.

We should also comment on similarities and difference between solutions derived for data sets $\mathcal{D}_1$ and $\mathcal{D}_2$ in this work, and with the Keplerian model in Benedict et al. (2022).

We obtained very similar eccentricities of the planets, particularly the innermost eccentricity constrained to $e_1 \simeq 0.1$. Given the old age of the star $\simeq 6.7$ Gyr and short orbital period $\simeq 9.64$ d of the warm Neptune, its eccentricity might be tidally circularized. We conducted direct numerical integrations of the system with all planets for a few Myr using the SABA$_4$ integrator (Laskar & Robutel 2001) with the step size of 0.5 d, and we did not detect such a large eccentricity which could be forced by interactions with the outer planets. Actually, HD 160691d seems to be a common example in the known sample of warm Neptunes that exhibit non-zero eccentricity, typically around 0.15 (Correia, Bourrier & Delisle 2020). They found mechanisms opposing gravitational tides, such as thermal atmospheric tides, evaporation of the atmosphere, and the eccentricity excitation from a distant companion. The later seems to be not the cause of the moderate eccentricity of HD 160691d, but the presence of atmospheric tides may be sufficient to explain its moderate value.

The most significant difference between the solutions in Benedict et al. (2022) and in this work is relatively shorter orbital period of

Table 2. Best-fitting parameters of the μ Arae (Cervantes) system for the Keplerian (Fits IIK) and Newtonian (Fits IIN) parametrization, data set $\mathcal{D}_2$. The osculating epoch is the date of the first observation in the UCLES data set. The system is coplanar with the inclination $I = 90°$ and nodal longitudes $\Omega = 0°$. The stellar mass is $1.13\,\mathrm{m}_\odot$ (Bonfanti et al. 2015) as used by Benedict et al. (2022), and close to $1.10 \pm 0.02\,\mathrm{m}_\odot$ in (Soriano & Vauclair 2010). The RV offsets are computed w.r.t. the mean RV in each individual data set. Uncertainties are estimated around the median values μ, i.e. $[\mu - \sigma, \mu + \sigma]$ as the 16th and 86th percentile of the samples. Numerical values for Fit IIN selected from MCMC samples with low RMS are quoted to the 7th digit after the dot, to make it possible to reproduce the dynamical maps and direct numerical integrations. The mean longitude $\lambda = \varpi + \mathcal{M}$ at the epoch was computed from the MCMC samples.

| Planet	HD 160691d (Dulcinea, 1)	HD 160691e (Rocinante, 2)	HD 160691b (Quijote, 3)	HD 160691c (Sancho, 4)
	Fit IIK (Keplerian model of the RV, data set $\mathcal{D}_2$, RMS = $3.4\,\mathrm{m\,s^{-1}}$)			
$K\,(\mathrm{m\,s^{-1}})$	2.84 ± 0.17	12.36 ± 0.30	35.81 ± 0.20	22.7 ± 0.26
P (d)	9.638 ± 0.001	308.36 ± 0.29	644.92 ± 0.29	4019 ± 24
$e\cos\varpi$	-0.052 ± 0.037	-0.073 ± 0.014	0.036 ± 0.011	-0.001 ± 0.011
$e\sin\varpi$	-0.024 ± 0.040	-0.012 ± 0.017	0.025 ± 0.008	0.054 ± 0.011
e	0.071 ± 0.034	0.076 ± 0.014	0.045 ± 0.008	0.055 ± 0.011
ϖ (deg)	204 ± 41	189 ± 13	$35.1 \pm (14.3, 12.6)$	91 ± 12
$\mathcal{M}$ (deg)	$225 \pm (41, 44)$	62 ± 13	$258.3 \pm (12.5, 14.3)$	147 ± 11
λ (deg)	69.0 ± 10.5	250.7 ± 4.1	293.4 ± 0.9	237.7 ± 1.9
$V_0\,(\mathrm{m\,s^{-1}})$	CORALIE: -7.36 ± 1.10, UCLES: 0.77 ± 0.25, HARPS: 2.12 ± 0.20			
$\sigma_f\,(\mathrm{m\,s^{-1}})$	CORALIE: 5.33 ± 0.99, UCLES: 0.68 ± 0.49, HARPS: 1.80 ± 0.14			
	Fit IIN (Newtonian model of the RV, data set $\mathcal{D}_2$, RMS = $3.4\,\mathrm{m\,s^{-1}}$)			
$m\sin I\,(m_{\mathrm{Jup}})$	0.032 ± 0.002	0.448 ± 0.011	1.65 ± 0.009	1.932 ± 0.022
	0.0297566	0.4558348	1.6608084	1.9478583
a (au)	$0.092319 \pm 5 \times 10^{-6}$	0.9347 ± 0.0015	1.522 ± 0.001	5.204 ± 0.021
	0.0923174	0.9342193	1.5209196	5.2065203
$e\cos\varpi$	-0.065 ± 0.050	-0.047 ± 0.013	0.035 ± 0.011	-0.003 ± 0.011
$e\sin\varpi$	-0.034 ± 0.050	-0.026 ± 0.014	0.019 ± 0.008	0.047 ± 0.011
e	0.090 ± 0.042	0.055 ± 0.014	0.041 ± 0.009	0.049 ± 0.011
	0.0172379	0.0447130	0.0423168	0.0242568
ϖ (deg)	$207 \pm (39, 41)$	$209 \pm (13, 14)$	$28 \pm (16, 13)$	94.1 ± 13.4
	285.3319635	215.5470967	14.4134097	88.4886424
$\mathcal{M}$ (deg)	$221 \pm (40, 44)$	$45 \pm (16, 15)$	$265 \pm (14, 16)$	145 ± 13
	147.4681451	39.3680159	276.3668580	150.2821658
λ (deg)	71 ± 10	254.6 ± 4.4	293.0 ± 1.0	239.0 ± 1.9
$V_0\,(\mathrm{m\,s^{-1}})$	CORALIE: -7.2 ± 1.1, UCLES: 0.87 ± 0.26, HARPS: 2.25 ± 0.19			
$\sigma_f\,(\mathrm{m\,s^{-1}})$	CORALIE: 5.3 ± 1.0, UCLES: 0.48 ± 0.42, HARPS: 1.69 ± 0.14			

HD 160691c, by $\simeq 100$ d (yet only $\simeq 2$ per cent) in Benedict et al. (2022). They report this solution as strongly unstable in 100 Kyr time-scale, in contrast to our models, which appear safely stable in extended regions of the parameter space, for at least 6.7 Gyr, as discussed below.

We attempted to address outlying UCLES measurements, visible on the right end of the observation window (Fig. 2). There are systematic deviations from the synthetic model, reaching $\simeq 10\,\mathrm{m\,s^{-1}}$, and unlikely they can be eliminated with the standard RV ephemeris. The HARPS and UCLES epochs overlap almost throughout the time window, but the HARPS measurements do not deviate as systematically as the UCLES data from the common model. This can be explained by a long-term instrumental UCLES effect. In order to account for it, we added a periodic drift to the Keplerian RV model for the UCLES data $\mathrm{RV}_{\mathrm{drift}}(t) = A\cos(nt + \phi_0)$, where A, n, and ϕ_0 are the semi-amplitude, frequency, and relative phase of the signal, respectively.

As the result of the MCMC sampling of the Keplerian model with this modification, we show (O–C) for the best-fitting model in Fig. 4 and a section of the corner plot for the posterior with offsets, error floors, and drift parameters (on-line Supplementary Material, Fig. S2). Note that in this case we analyzed only the concurrent HARPS and UCLES RV series (data set $\mathcal{D}_3$). It turns out that the drift component can significantly reduce the UCLES outliers. The drift correction reduces the RMS value to $2.5\,\mathrm{m\,s^{-1}}$, which is almost

$1\,\mathrm{m\,s^{-1}}$ less than the value for the unmodified model. However, the posterior distributions reveal that the drift's long period $P = 2\pi/n \simeq 36$ yr cannot be meaningfully constrained. Moreover, its half-amplitude $A \simeq 12$–$15\,\mathrm{m\,s^{-1}}$ is weakly limited on the right end, and strongly correlated with the RV offset $V_{0,2} \equiv V_{0,\,\mathrm{UCLES}}$, as it is labeled in the corner plot for the UCLES data. At the same time, the orbital parameters have not changed except for the period of $P_4 \simeq (3944 \pm 27)$ d, significantly shorter than $P_4 \simeq 4020$–4060 d in our models without drift, but similar to $P_4 \simeq 3947$ d in the solution of Benedict et al. (2022).

Given some variability in the residuals to the Keplerian and Newtonian models in Fig. 2, we analyzed them with the Lomb–Scargle periodogram, in the period window from 2 d to $64\,000$ d. The results are shown in Fig. 4. Indeed, the (O–C) in the left-hand panel for the Keplerian 4-planet model to the data set $\mathcal{D}_2$ shows some signature of the long-term drift. However, we did not detect any significant peak at the 1 per cent false alarm probability estimated by the bootstrap method at a level of $\simeq 0.07$. We performed the same test on the residuals to the Keplerian 4-planet model with sinusoidal drift added to the UCLES data. It is clear that the long-term drift period has disappeared, and there are still no significant peaks in the high frequency range. The (O–C) analysis suggests that we could not detect any significant RV signal that can be attributed to a new planet in the system.
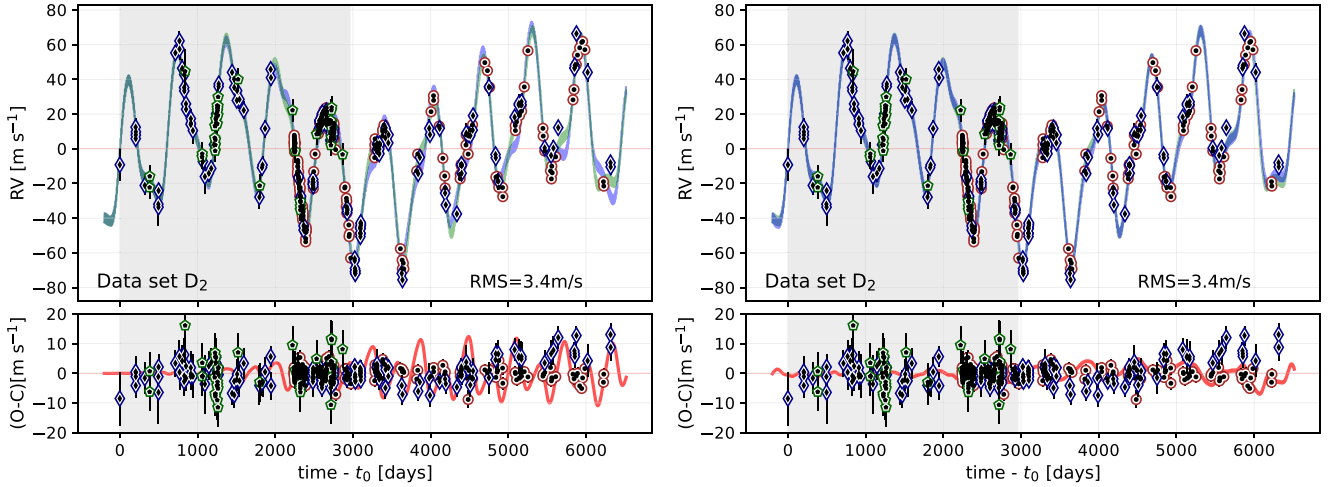
Figure 2. Left-hand panel: synthetic curves of the best-fitting Keplerian model to $\mathcal{D}_2$ data set, depicted as Fit IIK in Table 2 (light-green curve) and its Newtonian interpretation (light-blue curve) overplotted on the RV data. The difference between the RV signals illustrates a red curve in the residuals (O–C) panel for the Keplerian ephemeris. Symbols describe the RV measurements from different spectrometers: green pentagons are for CORALIE, brown/red circles are for HARPS and blue diamonds are for UCLES. Error bars in the (O−C) diagram include the error floor parameters. The shaded rectangle marks the time-span of the RV data in Goździewski et al. (2007) and Pepe et al. (2007). Right-hand panel: Synthetic curves of best-fitting Keplerian (light-green curve) and Newtonian models (light-blue curve) to $\mathcal{D}_2$ data set, depicted as Fit IIK and Fit IIN (Table 2), and overplotted on the RV data. The difference between the signals illustrates a red curve in the Keplerian residuals (O–C) panel. Parameters of the models correspond to the maxima of posterior samples. Symbols describe the RV measurements from different spectrometers: green pentagons are for CORALIE, brown circles are for HARPS and blue diamonds are for UCLES. Error bars in the (O–C) diagram include the error floor parameters, and the shaded region is the RV data span prior to the analysis conducted in 2006.

These results are consistent with the conclusions in the work of Benedict et al. (2022). They did not detect any correlation of the RV variability attributed to the planets with the periodicity of the spectral line profile distortion indicators. They found peaks of the bisector with low significance, around 357–368 and 497 d, which can be explained by stellar activity.

Since the inclusion of RV drift appears problematic due to the strong $V_{0,2}$–A correlation, and the drift-modified model does not actually qualitatively change the orbital architecture and stability of the system (as justified below), other than shortening the outermost orbital period by $\simeq 2$ per cent, we have abandoned this model. However, the likely instrumental nature and origin of the UCLES RV-outliers remains unexplained.

3 LONG-TERM STABILITY OF THE SYSTEM

The well bounded best-fitting parameter ranges make is possible to simplify the analysis of the dynamical character of the system. We conducted it with two fast dynamical indicators, the Mean Exponential Growth factor of Nearby Orbits (MEGNO, $\langle Y \rangle$; Cincotta et al. 2003) and the Reversibility Error Method (REM; Panichi et al. 2017). These numerical tools are CPU-efficient variants of the Maximal Lyapunov Exponent (MLE) that make it possible to detect unstable solutions and visualize the structure of the phase space.

The usefulness of the MEGNO method in analyzing the dynamics of planetary systems with strongly interacting companions has been proven for a long time (e.g. Goździewski et al. 2012, and references therein). We also shown in Panichi et al. (2017) that the REM indicator is not only equivalent to MEGNO, but may be also much more CPU-efficient. Briefly recalling the idea of this algorithm, computing REM relies in comparing the difference between the Cartesian initial condition $\mathbf{x}_0$ after integrating it numerically forward and back, for the same number n of time-steps Δt, using a time-

reversible numerical scheme, to obtain the final state $\mathbf{x}(\pm n \Delta t)$. Then the REM indicator is

$$\text{REM} = ||\mathbf{x}_0 - \mathbf{x}(\pm n \Delta t)||. \tag{6}$$

This difference grows exponentially with integration time for chaotic systems, and at a polynomial rate for regular (stable) configurations. Such a simple algorithm can be implemented with a symplectic discretization scheme. In practice, for systems with small and moderate eccentricities, which μ Arae systems appear to be, we use the classic leap-frog algorithm (e.g. Laskar & Robutel 2001) with symplectic correctors of the order 5 (Wisdom 2006), offering numerical accuracy and efficiency comparable to higher order methods (Wisdom 2018), see also Panichi et al. (2017) for details. As we have shown, in the later paper, this REM algorithm is particularly useful in regions of phase space with predominantly stable solutions and outperforms then any MEGNO variant in terms of CPU-efficiency.

In this work, to speed-up computations, we conducted the numerical simulations using our μFARM code parallelized with the Message Passing Interface (MPI). For the numerical integrations of the N-body equations of motion for individual ICs, we used the SABA$_4$ symplectic scheme (Laskar & Robutel 2001) as well as Everhardt's algorithm implemented in the REBOUND package (Rein & Spiegel 2015).

3.1 Stability of the model based on data set $\mathcal{D}_1$

We first computed the 2D dynamical maps in the neighbourhood of the Newtonian Fit IN in Table 1, based on the original data set $\mathcal{D}_1$ from Benedict et al. (2022). Fig. 6 illustrates the (a_3, e_3)–plane. In these scans, all other orbital elements are kept at their best-fitting values listed in Table 1. To make possible reproduce the results, we quote exact numerical values of the elements and masses. For each initial condition in the grid, the equations of motion were integrated
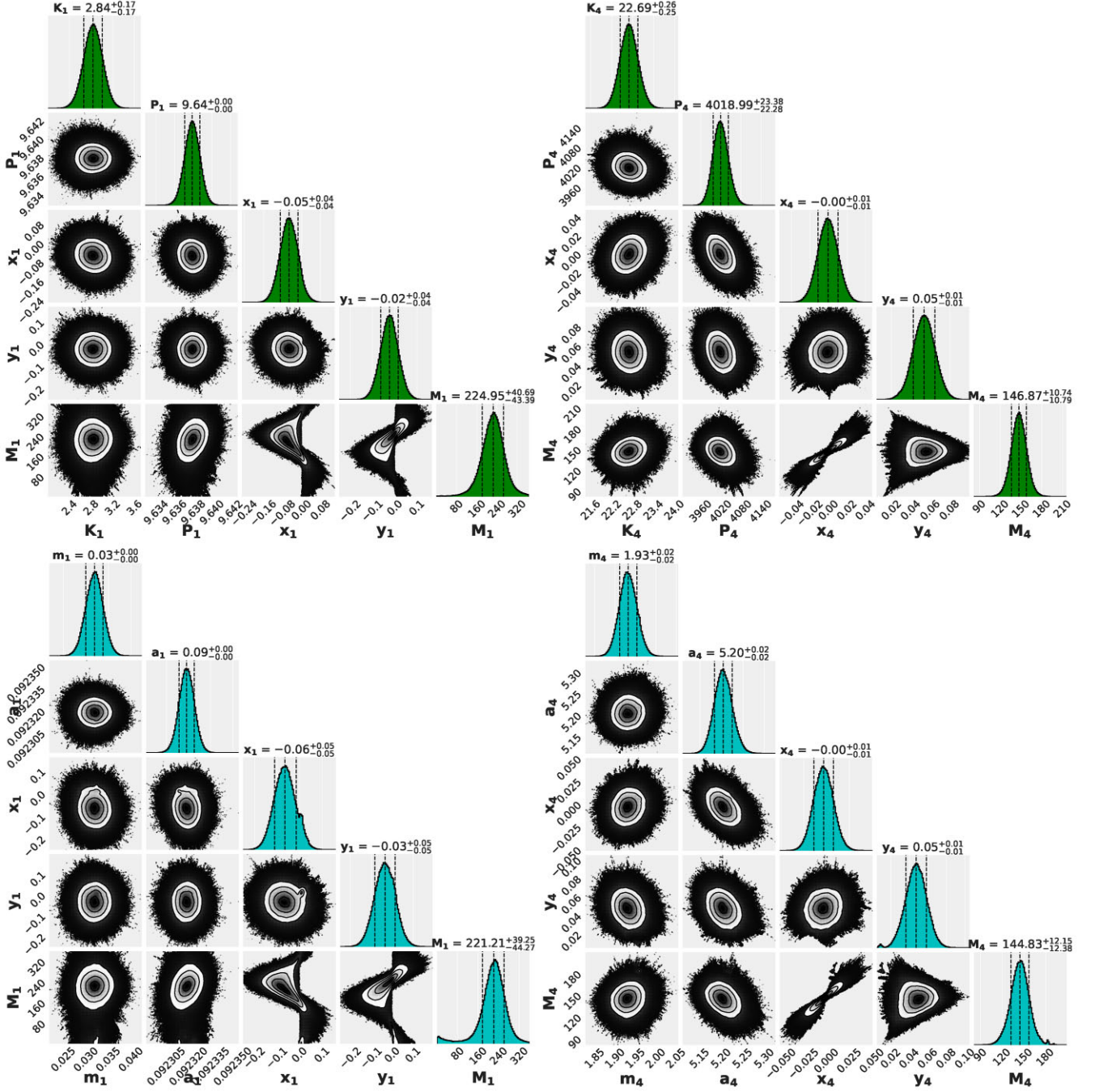
Figure 3. 1D and 2D projections of the posterior probability distribution for orbital parameters of the innermost (left column) and the outermost (the right column) planet, respectively. The top row is for the Keplerian model, and the bottom row is for the Newtonian model to data set $\mathcal{D}_2$. The parameters are expressed in units consistent with Table 2. The semi-amplitude K_i is equivalent to the mass m_i, and the orbital period P_i is equivalent to the semimajor-axis a_i. The MCMC chain length is 180 000 iterations for each of 384 different instances (walkers) selected in a small ball around a best-fitting solution found with the evolutionary algorithms for the Keplerian model, and 294 000 iterations in each of 176 walkers for the Newtonian model. Parameter uncertainties are estimated as 16th and 84th percentile samples around the median values at 50th percentile.

up to 200 Kyr, corresponding to $\simeq 1.8 \times 10^4 P_4$. This time interval allows for the detection of short-term chaotic motions for the time-scale of the MMRs instability (e.g. Goździewski & Migaszewski 2018).

Some of the dynamical maps were computed for 3-planet systems with the most massive planets, omitting the innermost warm Neptune. Its very short orbital period of 9.64 d compared to that one of the

outermost planet ($\simeq$4000 d) causes a huge CPU overhead. Before that, we investigated whether the presence of Dulcinea could affect the orbital evolution of the other massive companions and such 3-planet maps. To this end, we numerically integrated the systems described by Fit IN, with and without the warm Neptune, for several Myr, when secular effects may already play a role. Fig. 5 illustrates the resulting osculating semimajor and eccentricity over a narrow
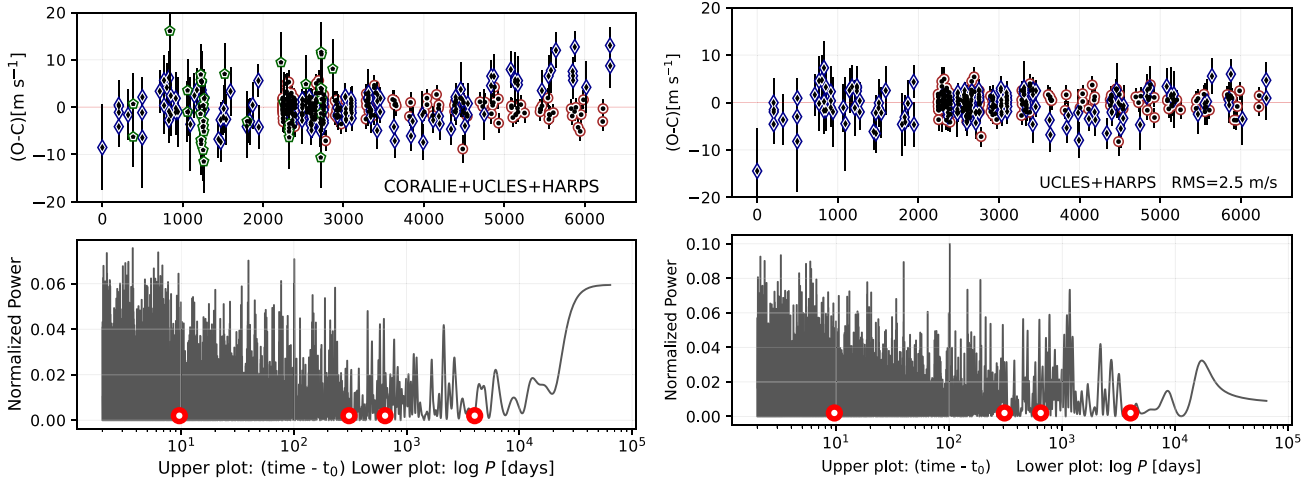
Figure 4. Lomb–Scargle periodograms for residuals to the Keplerian Fit IIK in Fig. 2 (left-hand panel, data symbols are the same as in Fig. 2) and to the residuals to the best-fitting Keplerian model with a hypothetical, instrumentally induced periodic term $A \cos(nt + \phi_0)$ in the UCLES measurements, over-plotted on the RV measurements from UCLES and HARPS spectrometers (right-hand panel). Brown circles are for HARPS and blue diamonds are for UCLES instrument, respectively. Red filled circles mark the orbital periods of the detected planets.
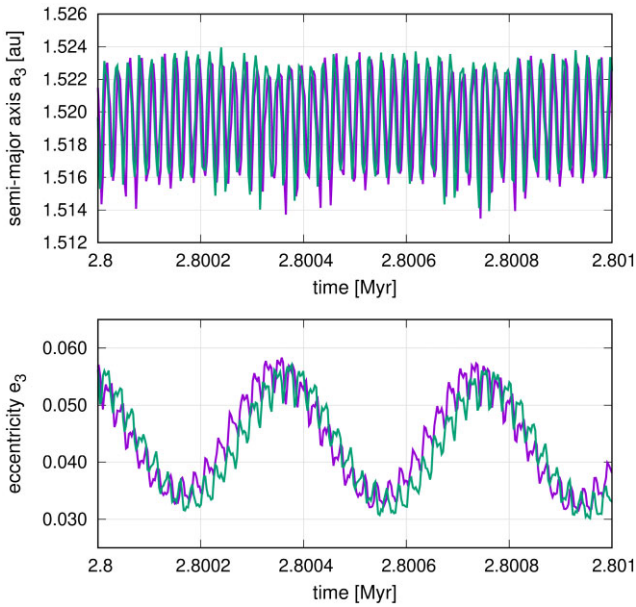
Figure 5. Temporal evolution of the osculating semimajor axis (top panel) and eccentricity (bottom panel) for planet HD 160691b in a narrow time window around 2.8 Myr. In each panel, curves with different colour illustrate solutions for two ICs, with and without the innermost planet. In the later case, we added its mass to the mass of the star. Elements of the planets included in the integrated system in both experiments are the same (Fit IN, Table 1). The systems were integrated with the SABA$_4$ symplectic scheme with the step size of 0.5 d.

time interval around 2.8 Myr for Quijote (HD 160691b). Clearly, the elements span the same ranges and evolve along curves with very similar shapes. Their de-phasing is due to a small change of the mean motion and other elements. The most significant shift can be seen for Sancho (HD 160691c, not shown here), yet its semimajor axes is shifted by $\simeq 0.002$ au, roughly 10 times less than 1σ uncertainty for this orbital element.

To study whether the innermost planet can be omitted from the system for long-term integrations, Farago, Laskar & Couetdic (2009)

averaged the model for the fast orbiting innermost planet. Obviously, such an analytical model is numerically as CPU efficient, as the 3-planet model. Moreover, they found for the particular μ Arae case the results from three formulations of the orbital evolution: the exact (averaged) one, the 3-planet model with omitted warm Neptune, and the 3-planet model with its mass added to the mass of the star lead to barely distinct results.

To test this independently, and without any simplifications of the equations of motion, we used the REM indicator directly and compared dynamical maps for the 3- and 4-planet configurations, respectively, for the same ranges of orbital parameters.

We start with the upper-left panel in Fig. 6 for a relatively broad region of the ICs marked with a star symbol. That map was computed without the innermost Neptune, using the leap-frog scheme and a time-step of 8 d. A wide structure around $a_3 \simeq 1.47$ au on the left of this IC corresponds to the 2b:1c MMR of the inner pair of Saturn–Jupiter-mass planets. Given the small 1σ uncertainty 0.001 au of the nominal semimajor axis, the separation of the best-fitting configuration from this MMR is meaningful (the error bars are smaller than the symbol radius). Simultaneously, the ICs is located between three narrow strips of unstable solutions that may be identified with higher order resonances. Close-up maps in the remaining panels of Fig. 6 reveal a very close proximity of the ICs to one of these strips.

Panels in the bottom row are for the same (a_3, e_3)-plane, but scanned with $\langle Y \rangle$ for the 3-planet model (bottom-left panel) and with REM calculated for the full 4-planet configuration (bottom-right panel), but with a much smaller step size of 0.33 d and lower resolution compared to the 3-planet REM-map computed with the leap-frog step-size 8 d (upper-right panel). Of course, this is forced by the short orbital period of HD 160691d. The maps clearly illustrate the one to one results, in a region with weakly unstable configurations and different, very fine dynamical structures. We may note that the ICs is negligibly shifted by $\simeq 10^{-5}$ au with respect to the unstable structure, between the 3-planet and 4-planet scans.

While the REM map for three planets was calculated several times faster than the $\langle Y \rangle$ map, the full REM calculation for four planets was more than 15 times slower per pixel. Such over-head is acceptable, however, given that the calculations were per-
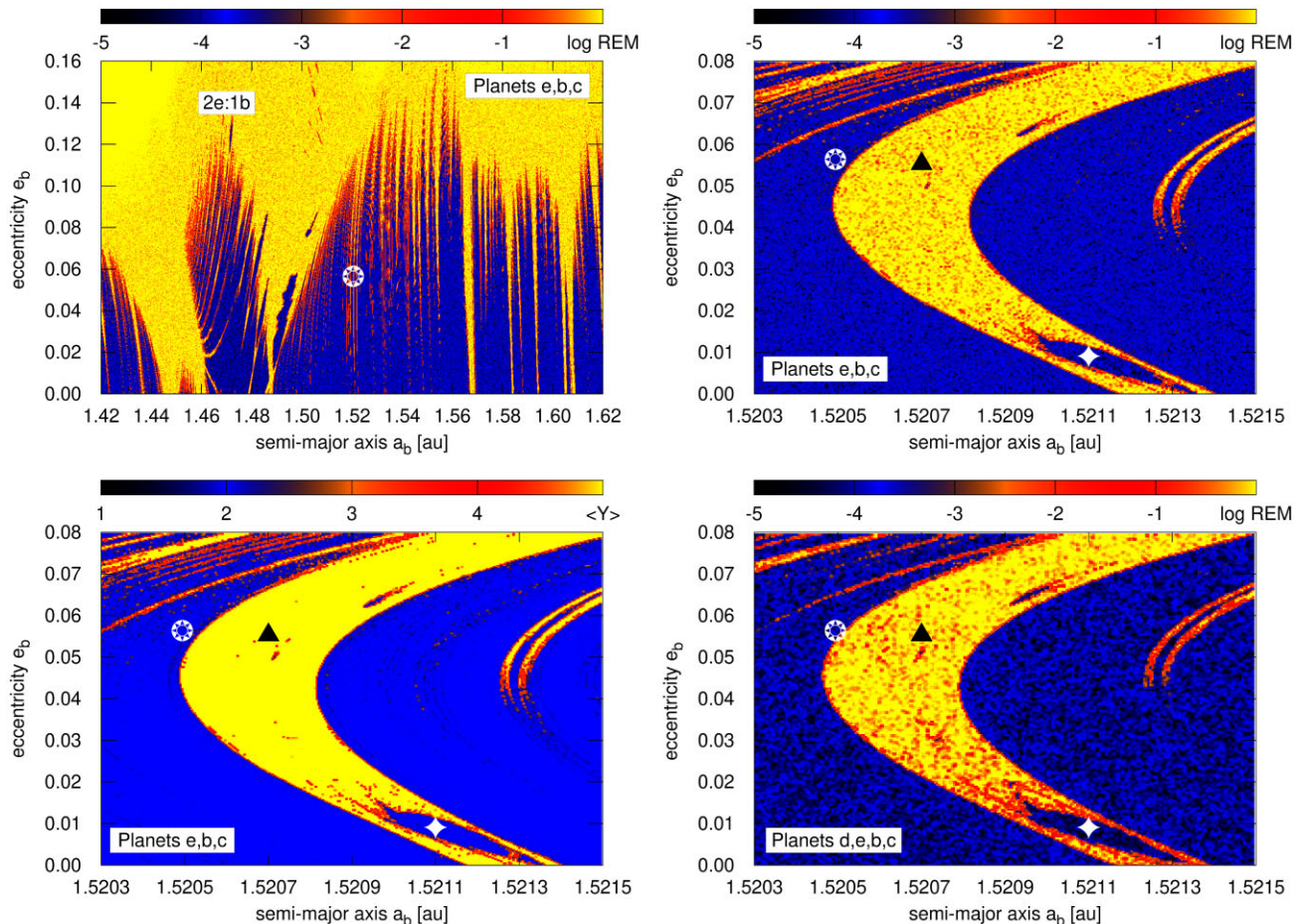
Figure 6. Dynamical maps for the best-fitting *N*-body Fit IN (Table 1) to data set $\mathcal{D}_1$. Top-right and bottom panels are for a close-up of the scan shown in top-left panel. The fast indicators $\log|\text{REM}| \lesssim -4$ and $\langle Y \rangle \simeq 2$ characterize regular (long-term stable) solutions, which are marked with black/dark blue colour; chaotic solutions are marked with brighter colours, up to yellow. The integration time of each initial condition is 200 Kyr ($\sim 1.8 \times 10^4 \times P_4$). Panels in the right column are for the 3-planet model omitting the warn Neptune, and for the full 4-planet configuration, respectively. The REM indicator was computed with the leap-frog with the step size of 8 d (3-planet map) and 0.33 d, respectively (bottom scan). The MEGNO scan (bottom-left panel) was computed for 3-planet model with the Gragg–Bulirsch–Stoer (GBS) algorithm (Hairer, Nørsett & Wanner 1993; Hairer & Wanner 1996). The asterisk symbol means the position of the nominal model. Diamond and triangle symbols are mark the ICs tested with the direct numerical integrations for 6.7 Gyr, see the text. Resolution for the top and bottom-left plots is 640×360 points, and 360×200 points for the bottom-right scan.

formed without any simplification of the Newtonian equations of motion.

The detection of fine unstable structures and tiny islands of stable resonances confirms once again a good sensitivity of the REM algorithm for stable and unstable solutions. To show this better, we interpreted the unstable strip structure through the numerical analysis of the fundamental frequencies (NAFF; Laskar & Robutel 2001) of a particular system marked with a white diamond symbol in a small stable island around $(a_3, e_3) \simeq (1.5211\,\text{au}, 0.01)$. This island is a part of the three-body MMR 2e:−4b:1c structure (one of the strips spanning $e_3 \in [0, 0.1]$). We plotted evolution of a selected critical angle of this resonance $\theta_{2:-4:-1} = 2\lambda_2 - 4\lambda_3 - \lambda_4 + \varpi_2 + \varpi_3 + \varpi_4$ in Fig. 7. This critical angle librates with large amplitude around $180°$, and the orbital configuration is perfectly stable for at least 1 Gyr, consistently with its location in the stable island.

In contrast, we selected formally unstable ICs by shifting the nominal semimajor axis to the right (to the unstable strip) and marked with a black triangle symbol (see close-up panels in Fig. 6). We integrated this ICs for 6.7 Gyr with the SABA$_4$ scheme and for
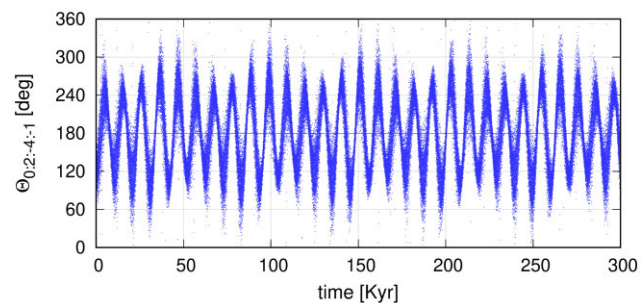
Figure 7. Evolution of a selected critical angle $\theta_{2e:-4b:-1c}$ of the three-body MMR of the outer planets for the initial condition marked in dynamical maps in Fig. 6 with a white diamond.

1 Gyr with the variable step-size IAS15 integrator. Also in this case the system does not reveal any signature of geometric instability, in spite of its formally chaotic character in the sense of MLE (it is not illustrated here, but we invoke a similar example in Section 3.2.2). The width of this third-order MMR is very small, $\Delta a_3 \simeq 0.003$ au,

and the diffusion is likely so slow that it does not lead to a change or disruption of the system.

We remark here that Benedict et al. (2022) found quite an opposite, catastrophic instability of the system. In their Keplerian solution, $P_4 \simeq (3947 \pm 23)$ d is apparently the only significant difference with our fits (Table 1). The origin of this discrepancy may be a subtly different parametrization of the RV signal. For instance, Benedict et al. (2022) did not fit the jitter uncertainties as free parameters, but tuned it posteriori for each data set to obtain $\chi_\nu^2 \simeq 1$. Moreover, our models yield smaller RMS $\simeq 3.4$ m s^{-1} rather than $\simeq 3.8$ m s^{-1} in the prior work. A shorter period of $P_4 \simeq 3947$ d may be pointing to an unstable structure close to $a_4 \simeq 5.12$ au (similar to that one visible in the top-left panel in Fig. 10). We integrated the system with the outermost planet Sancho placed in this unstable zone, but the system survived for at least 1 Gyr. We could not reproduce the strong instability reported in (Benedict et al. 2022), and we cannot find any convincing explanation of this discrepancy.

### 3.2 Stability of the Newtonian model based on data set $\mathcal{D}_2$

As mentioned above, we also conducted the GEA and MCMC analysis for data set $\mathcal{D}_2$. The results are very similar to the $\mathcal{D}_1$ case. However, there are some subtle qualitative changes with respect to the models for $\mathcal{D}_1$. The eccentricities of the Jovian planets tend to be systematically even smaller than for the $\mathcal{D}_1$-systems. Also the semimajor axes and orbital periods locate the systems in even more 'safe', stable zone displaced from the 6b:1c MMR by more than 0.1 au, which corresponds to $\simeq 5\sigma$ in terms of the semimajor axis uncertainty.

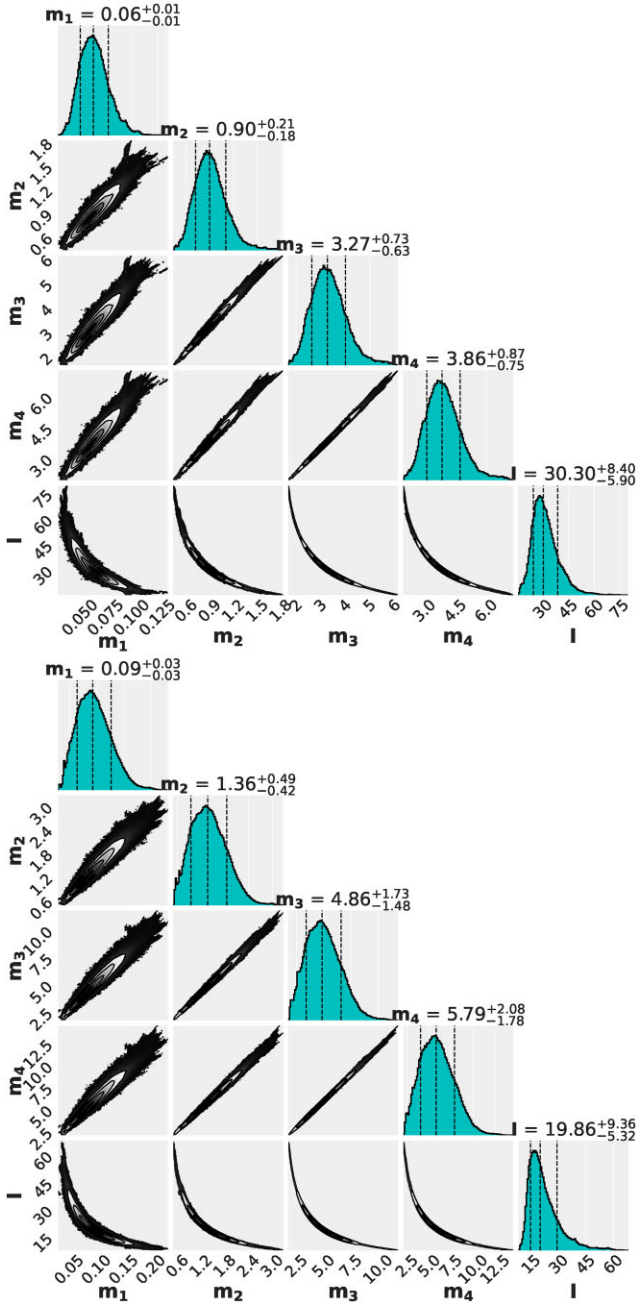#### 3.2.1 The 2e:1b MMR proximity

Goździewski et al. (2007), Pepe et al. (2007) and Farago et al. (2009) investigated the proximity of the inner pair HD 160691e-b to the 2e:1b MMR. In the two later papers, they found the best-fitting model close to the separatrix, unstable zone of this resonance. Contour levels of χ_ν^2 encompass both the near-resonance and the resonant configuration (Pepe et al. 2007, their fig. 7). In Goździewski et al. (2007), we also found that the relative position of the ICs and the shape of the 2e:1b resonance in the (a_3, e_3)-plane strongly depend on the semimajor axis of HD 160691c that could be only weakly constrained to ± 1300 d (4–7 au) and eccentricity e_4 as large as 0.2 at the time.

We can now revisit this issue with a significantly updated Fit IIN. To do so, we calculated the dynamical maps illustrated in Fig. 8 for the 3-planet (upper panel) and 4-planet (middle panel) configurations, respectively. For the 3-planet model, we added the mass of innermost Neptune to that of the star. It can be clearly seen that the two maps coincide in each detail, and any shift in the position of the ICs relative to the fine structures is barely noticeable.

The coordinates of the dynamical maps were chosen to match the NAFF maps in (Pepe et al. 2007, their fig. 7) and in (Farago et al. 2009, their fig. 3). Since a direct comparison of the maps is not possible, due to changes in elements in the ICs, we have marked with a diamond a qualitative position of the former initial state relative to the approximate shape of MMR 2e:1b and its separatrix zone. Clearly, the Fit IIN is shifted from the separatix border by $\simeq 5\sigma$. This statistically proves that the nominal system is not resonant and is in a safely stable zone. The narrow stripes of unstable motions can be identified with weak, higher-order 3-body MMRs with very long diffusion time-scales, similar to the 2e:-4b:-1c MMR analyzed above.
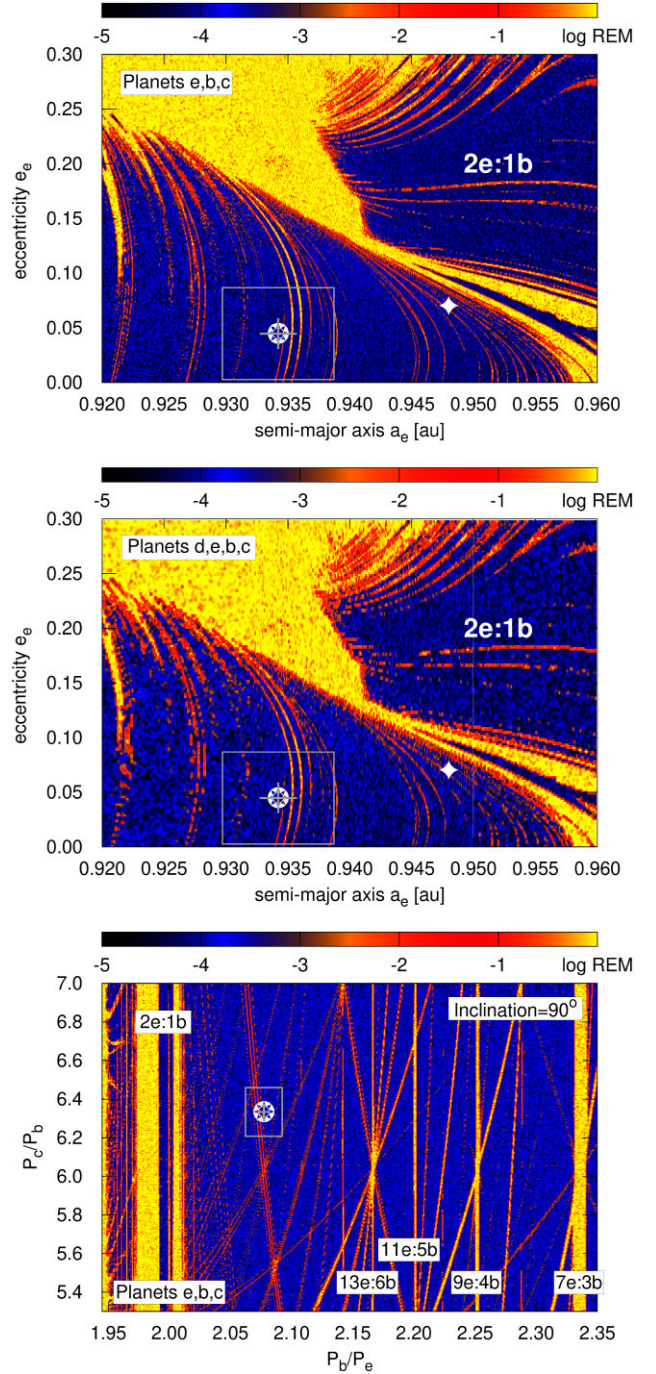
Figure 8. Dynamical maps for Newtonian Fit IIN (Table 2) to data set $\mathcal{D}_2$. The REM with log |REM| $\lesssim -4$ characterize regular (stable) solutions marked with black/dark blue colour; chaotic solutions are marked with brighter colours. The integration time of each ICs is 200 Kyr ($\sim 1.8 \times 10^4 \times P_4$). The top panel is for 3-planet model (the warm Neptune's mass added to the star mass), and the middle panel is for all planets. The bottom panel is for the REM scan in the plane of Keplerian period ratios, for 3-planet model. The REM was computed with the leap-frog with the step size of 8 d for 3-planet, and 0.33 d for 4-planet scans, respectively. The asterisk marks the nominal ICs and diamond marks the qualitative position of the ICs in Pepe et al. (2007), see their Fig. 7. Resolution for the top plot is 1140×360, 560×200 for the middle plot, and 720×720 pixels for the bottom plot. The cross centred at the ICs marks 1σ error bars (0.0015 au, 0.014) for the (a_2, e_2)-plane, as in Table 2, and for the period ratios (0.005,0.042)-plane, respectively. The grey rectangles are for 3σ region.

These conclusions can be reinforced with a REM map for the three outer planets in the semimajor axes space, represented in the orbital period ratios (P_3/P_2, P_4/P_3)-plane, as the astrocentric Keplerian description of the semimajor axes, see the bottom panel of Fig. 8. Here, we marked 1σ and 3σ uncertainties the same as in the previous panels. We computed them based on the MCMC samples. In this map, the 2-body MMRs are marked with vertical (some of them labelled) and horizontal curves. Skewed curves and lines are for 3-body MMRs and could be identified with a method described in (Guzzo 2005). Also this REM map reveals the Fit IIN safely separated from the 2e:1b MMR by several σ.

3.2.2 Stability limits depending on inclination

Finally, we performed direct MCMC sampling with the inclination added as a free parameter to the Newton co-planar model. As expected, since the RV time series are relatively short covering $\simeq$ 1.5 periods of the outermost planet, the inclination may be only weakly constrained in the assumed interval $[5°, 90°]$. There should be also strong, almost linear correlations between the masses and mass-inclination correlation due to the $m\sin I$ degeneracy.

However, this intuition seems insufficient in light of the MCMC sampling results for data set $\mathcal{D}_2$, illustrated in Fig. 9 (upper plot). It shows posterior histograms for all masses $m_{1, 2, 3, 4}$ and for the inclination I as a free parameter. In addition to the predicted strong mass-inclination correlation, we found a clear, well-defined posterior maximum for $I \simeq 30°$. We tested this effect in multiple MCMC sampling experiments, varying the initial solution and sampling conditions.

Since, due to parameter correlations, the estimated autocorrelation time is as many as 25,000 iterations, we sampled up to 400 000 steps for each of 144 walkers, corresponding to 15–20 autocorrelation times. As a starting point for the sampling, we took Fit IIN in Table 2 supplemented with $I = 20°$, $45°$, $60°$, and $75°$, respectively. Interestingly, in all cases, regardless of the initial I, the extremum is robust and occurs around $I \simeq (30° \pm 10°)$. At the same time, we monitored the RMS $>3.4\,\mathrm{m\,s^{-1}}$ for best-fitting solutions, which rises significantly to RMS $\simeq 3.6$–$3.8\,\mathrm{m\,s^{-1}}$ below $I > 30°$. This means that the RV data predicts all planetary masses safely below the brown dwarf limit, i.e. the physical masses can be at most 2–3 times the minimum masses.

To assess the statistical significance of this result, we computed the Bayesian information criterion (BIC) defined as (e.g. Claeskens & Hjort 2008)
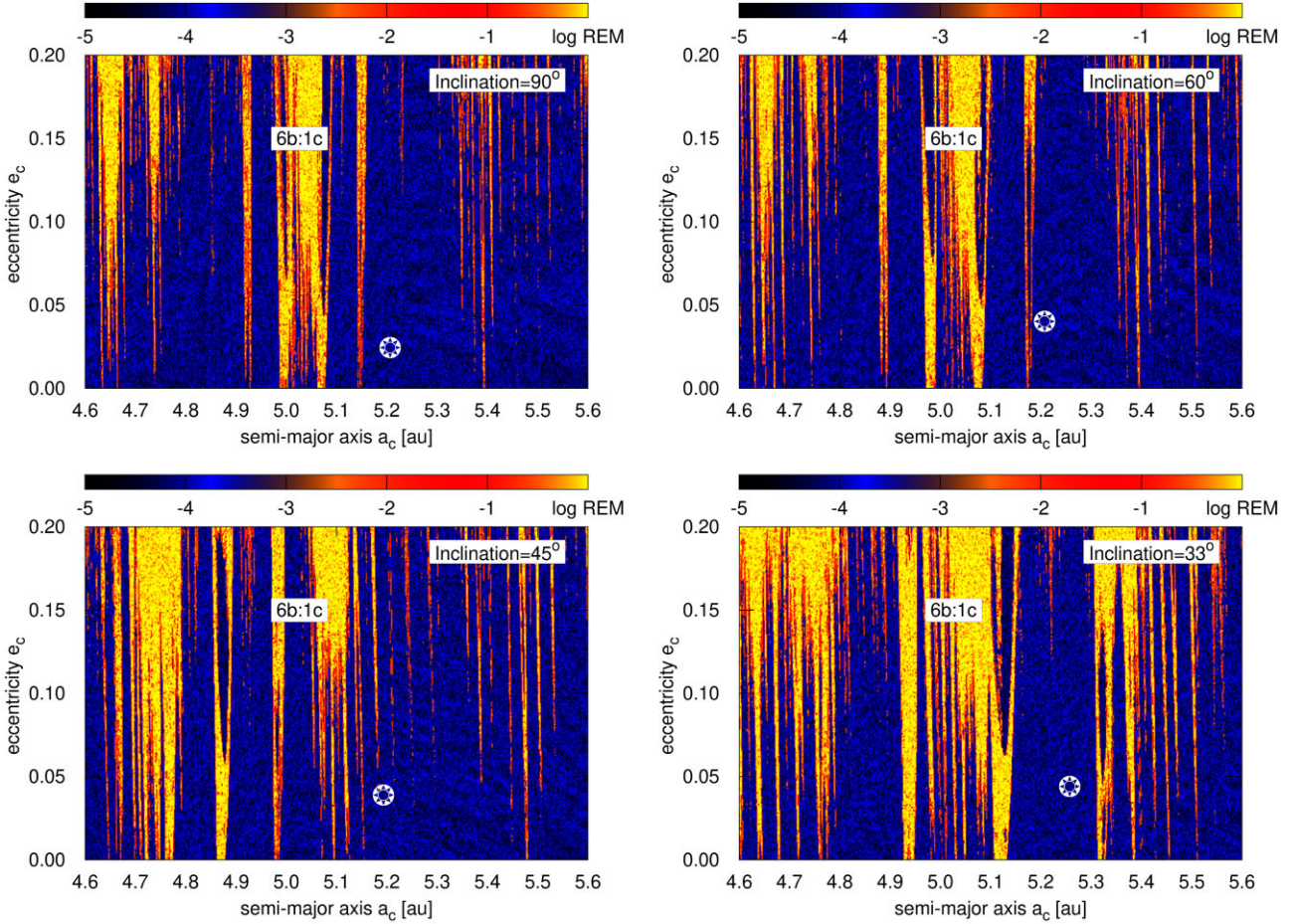
$$\mathrm{BIC} = p \ln N_{\mathrm{RV}} - 2 \ln \mathcal{L}_{\mathrm{max}},$$

for the Newtonian model, for the edge-on system with $I = 90°$ and for a model with variable I, with $p = 26$ and $p = 27$ of free parameters, respectively; $N_{\mathrm{RV}} = 411$, and $\ln \mathcal{L}_{\mathrm{max}}$ is the value of $\ln \mathcal{L}$ evaluated at the posterior extremum. For the two models, we found $\ln \mathcal{L}_{\mathrm{max}}(\boldsymbol{\theta}, I = 90°) = -987.07$ and $\ln \mathcal{L}_{\mathrm{max}}(\boldsymbol{\theta}, I) = -987.7$, respectively, hence $\mathrm{BIC}(\boldsymbol{\theta}, I = 90°) = 2130.62$, and $\mathrm{BIC}(\boldsymbol{\theta}, I) = 2137.96$, respectively. Therefore

$$\Delta\mathrm{BIC} = \mathrm{BIC}(\boldsymbol{\theta}, I = 90°) - \mathrm{BIC}(\boldsymbol{\theta}, I) \simeq -7 < 2,$$

indicating that there is no evidence of the model with free inclination against the edge-on model with a smaller value of BIC, see Claeskens & Hjort (2008). However, if we apply the second-order Akaike information criterion (AIC) for small sample sizes ($N_{\mathrm{RV}}/p \simeq 15 < 40$),

$$\mathrm{AIC} = 2p + 2(p + 1)/(N_{\mathrm{RV}} - p - 1) - 2 \ln \mathcal{L}_{\mathrm{max}},$$

Figure 9. 1D and 2D projections of the posterior probability distribution for the planet masses and the system inclination, illustrating MCMC samples for the Newtonian model fitted with I as a free parameter. Upper plot: The result for data set $\mathcal{D}_2$. The MCMC chain length is 400 000 iterations ($\simeq$15 times the greatest autocorrelation time) in each of 144 different instances selected in a small ball around Fit IIN (Table 2), completed with $I = 45°$. Lower plot: The result for data set $\mathcal{D}_3$ composed of HARPS and UCLES measurements. The MCMC chain length is 500 000 iterations in each of 144 different instances selected in a small ball encompassing Fit IIN (Table 2) computed for the osculating epoch in the middle of the data window and completed with the initial value of $I = 45°$. Parameter uncertainties are estimated as 16th, and 84th percentile samples around the median values (50th percentile) and marked with dashed lines on the 1-dim histograms. Masses $m_{1, 2, 3, 4} \equiv m_{\mathrm{e, d, b, c}}$ expressed in Jupiter masses, and the inclination I in degrees.

Figure 10. Dynamical maps for the best-fitting coplanar *N*-body Fit IIN (Table 2) to data set $\mathcal{D}_2$, extended to the inclination *I* space. Subsequent panels are for solutions selected from MCMC samples for the Newtonian model with varied inclination *I*, illustrated in Fig. 9, upper plot. The colour scale is the same, as in Fig. 6. The integration time of each initial condition is 300 Kyr ($\sim 2.7 \times 10^4 \times P_4$); we used the leap-frog scheme with the step size of 8 d. The asterisk symbol means the elements of the nominal fits. The inclination of the orbital plane is described in the top-right corner of each panel. An approximate position of the 6b:1c MMR is labeled. Resolution of the plots is 720×360 points.

then $\Delta\text{AIC} < 2$ for the two concurrent fit models, and that the candidate model is indicated almost as good as the best edge-on model (Claeskens & Hjort 2008). We consider this as a marginal indication of the significance of the inclined model, which needs to be addressed with longer RV time series.

Furthermore, we examined this effect for the $\mathcal{D}_3$ data set, consisting of only the most accurate HARPS and UCLES RVs, and also changed the osculating epoch of the Newtonian model to the middle of the RV time series. In this experiment, we also increased the number of iterations to 500 000 steps for each of the 144 walkers. As a starting ICs, we chose Fit IIN from Table 2 with an initial value of $I = 45°$, but without any prior tuning of this solution. The results are shown in Fig. 9, lower plot. In this case, the posterior distribution is shifted toward $I = 20°$. This may further indicate a systematic but weak dependence of the Newtonian model on the inclination, which is also sensitive to the RVs changes.
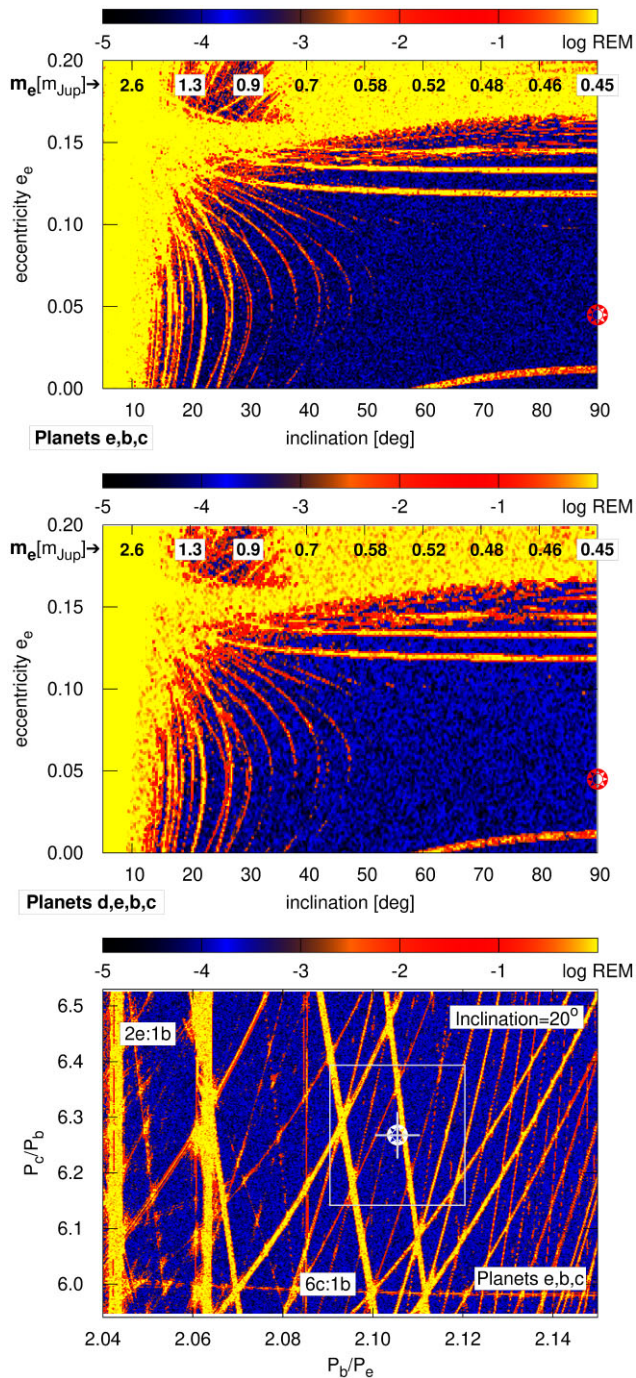
The stability zone and fine unstable structures for inclined coplanar systems are illustrated in dynamical maps in the (a_4, e_4)-plane (Fig. 10) constructed for different inclinations of the co-planar system. We selected the best-fitting solutions from the MCMC samples with lowest RMS $\simeq 3.35\,\text{m s}^{-1}$ detected, and close to particular, a'priori fixed inclinations. Subsequent panels are for such best-fitting models with the inclination equal to $I = 90°$ (the nominal

Fit IIN in Table 2), $I = 60°$, $I = 45°$, and $I = 33°$, respectively. In the later case, the planet masses are twice as large as in the nominal, edge-on system. Moreover, the orbital elements selected from the MCMC samples are slightly different, thus introducing variability consistent with parameter uncertainties to the elements behind the map coordinates.
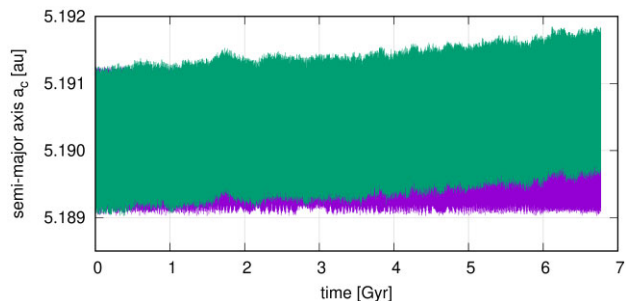
To effectively illustrate the region of stability with respect to *I* in a more global way, we scaled the minimal masses in Fit IIN according to the minimum mass rule $m_i \sin I = \text{const}$, recalling the mass-inclination correlation. We then calculated the dynamical maps in the (I, e_2) plane (Fig. 11). For reference, the second upper *x* axis in these maps is for the mass of HD 160691e scaled with $\sin I$.

Although, as we have shown, the influence of the warm Neptune is negligible for the dynamical evolution of the outer planets when their masses are minimal, this may not be the case for small inclinations. We therefore calculated two versions of the REM maps, for three- (top panel) and four-planets (middle panel), respectively (the later with lower resolution to save CPU time). It can be clearly seen that in the range of $I \in [5°, 90°]$, which covers the variation of masses spanning one order of magnitude, all, even very fine features of the phase space remain the same.

Finally, we constructed a REM map in the orbital period ratios plane shown in Fig. 11 (bottom panel) around $I = 20°$, similar

Figure 12. Time-evolution of the semimajor axis of HD 160691c (drawn in magenta) for the nominal system marked in the lower panel of Fig. 11 with the star symbol, and for a system shifted to the nearby unstable 3-body MMR structure (drawn in green) respectively. The configurations were integrated with SABA$_4$ scheme and the step size of 16 d for 6.7 Gyrs. Chaotic diffusion for the unstable resonant model is apparent. (The ICs for this model is given in the Supplementary Material on-line).

to the scan in Fig. 8. In this case, the masses of the planets are $(1.34, 4.91, 5.85)$ m$_{\rm Jup}$, i.e. the minimum masses scaled by a factor 3. We integrated each point for 300 kyr forward and back with the leap-frog scheme and the step size of 8 d. The ICs is located in a denser network of 2-body and 3-body MMRs, but still well separated from the 2e:1b MMR. We can also observe the high sensitivity of REM to interacting MMRs, indicated by in their regions of overlap (crossings).

Since the ICs is very close to an unstable 3-body MMR, we performed a comparative integration of the nominal system and a configuration slightly shifted so that it is located in this nearby unstable MMR region (yellow strip in the lower panel of Fig. 11). We used the SABA$_4$ scheme and the step size of 16 d, keeping the energy integral to 10^{-10} on the relative scale. In both cases, the system survived integrations for the lifetime of the star (6.7 Gyr). Such narrow chaotic 3-body MMRs, similar to that one analysed in Fig. 4 do not appear 'dangerous' for the long-term stability. The chaotic configuration reveals only weak diffusion of a_4 and e_4. This is illustrated in Fig. 12.

The general conclusion of this experiment is a relatively wide stable zone preserved despite the enlarged minimal masses of the planets 2–3 times. The limit of stable solutions for $I = 15°$–$20°$ roughly coincides with the shape of statistically detected posterior extremum for $I = 30°$ (data set $\mathcal{D}_2$) and $I = 20°$ for data set $\mathcal{D}_3$, as we found with the MCMC sampling. Systems with the most probable inclinations $I = 60°$ in purely random sample would be in the middle of a broad, stable zone. Such the likely inclination increases the planet masses by only 15 per cent.

Moreover, the clear posterior maxima for $I \simeq 30°$ and $I \simeq 20°$ found here (still, in the stable zone) may confirm the marginally detected bias toward small inclinations of multiple systems, investigated with the *HST* astrometry in Benedict et al. (2022). We should also note that for µ Arae very small inclinations $I \lesssim 10°$ can apparently be ruled out on both statistical as well as on dynamical grounds.

4 POSSIBLE DEBRIS DISCS AND SMALLER PLANETS

Based on the updated, rigorously stable and well-constrained orbital solutions collected in Table 2, we simulated the dynamical structure of hypothetical debris discs in the system. In the large 'gap' between the two outer planets, at $\simeq 1.52$ and 5.2 au, respectively, we can predict orbitally stable objects with masses that are below the present

Figure 11. REM dynamical maps for the *N*-body Fit IIN (Table 2) to data set $\mathcal{D}_2$, and planet masses scaled with $m \sin I$ rule. Values log $|$REM$| \lesssim -4$ are for long-term stable solutions marked with black/dark blue colour; chaotic solutions are marked with brighter colors, up to yellow. For the top and middle panels, the integration time of each ICs is 200 Kyr ($\sim 1.8 \times 10^4 \times P_4$), and for the bottom panel it is 300 Kyr ($\sim 2.7 \times 10^4 \times P_4$). The top panel is for the 3-planet model with the mass of the warm Neptune added to the mass of the star, and the middle panel is for all 4-planets, respectively. The upper axis marks the mass of m_2 rescaled according to the $m \sin I$ rule. The bottom panel is for the REM map in the orbital period ratios (P_3/P_2, P_4/P_3)-plane, around the nominal ICs found for $I \simeq 20°$, close to the posterior maximum in Fig. 9, bottom plot. Some MMRs are labelled. The REM indicator was computed with the leap-frog step size of 8 d for 3-planet and 0.33 d for 4-planet scans, respectively. Resolution is 640×360, 360×200, and 512×512 for the subsequent plots, respectively.

detection levels. This region may be an analogue of the Main Belt in the Solar system, given the striking similarity of the orbits of the Saturn- and Jupiter-mass planets to those of Mars and Jupiter. The second debris disc, located beyond the orbit of the outermost Jovian planet (Sancho), may be similar to the Kuiper Belt. There is also free space between the two innermost planets that may contain Earth-mass objects, in the wide free space extending for $\simeq 0.9$ au between the orbits.

We could try to recover the structure of the phase space using fast indicators, in the form of the dynamic maps shown earlier in Figs 6 and 10 for the planets. However, such maps constructed for fixed orbital phases of test particles permitted to vary freely may reveal an incomplete picture. The stability of a free test body in a system depends not only on its semimajor axis and eccentricity (a_0, e_0), but also on its relative orbital phase with respect to massive planetary perturbers.

To circumvent this limitation, we introduced a concept of the so-called $\langle Y \rangle$-model (or $\langle Y \rangle$-disc) (Goździewski & Migaszewski 2018). We assume that the massive planets form a system of primaries in safely stable orbits robust to small perturbations. Then we inject bodies with masses significantly smaller than masses of the primaries on orbits with different semimajor axes and eccentricities spanning the interesting region, and the orbital phases selected randomly. Next, we integrate numerically the individual synthetic configurations and determine their stability with the MEGNO aka $\langle Y \rangle$ fast indicator. For this experiment MEGNO is preferable over REM since we may expect that most of the orbits are unstable. As soon as MEGNO reaches a value $\langle Y \rangle \simeq 5$, sufficiently different for $\langle Y \rangle \simeq 2$ for stable solutions, we can stop the integration, thus saving CPU-time. We explain in detail the method and calibration experiments spanning orbital evolution of debris disks in the massive four-planet HR 8799 system for up to 70 Myr in Goździewski & Migaszewski (2018). A comparison of the results of direct numerical integrations with the outcomes of the $\langle Y \rangle$-model confirms that these two approaches are consistent one with the other. Yet the $\langle Y \rangle$-disc method is CPU-efficient and therefore makes it possible to obtain a clear, quasi-global representation of the structure of stable solutions. This algorithm is especially effective for strongly interacting systems.

To conduct the $\langle Y \rangle$ simulations, we chose Fit IIN located in a wide zone of stable motions. Such a 'safe' neighbourhood is important for the $\langle Y \rangle$-model, since the system is not prone to small perturbations exerted by the probe objects – we integrate numerically the orbits of all bodies. Again, since we focus on the space beyond the orbit of HD 160691e, $a_0 \simeq 0.9$ au, we omitted the innermost planet influence for the Main Belt and Kuiper Belt disks, to improve the CPU performance. However, the effect of the innermost planet was included in the simulation of the dynamical map for the inner zone between the warm Neptune and the Saturn-like planet (upper left panel in Fig. 13).

We considered three types of probe objects in different mass regime: Vesta-like asteroids with a mass of $3 \times 10^{-7}\, m_{\rm Jup}$, massive Earth-like planets with a mass of $10^{-2}\, m_{\rm Jup}$, and super-Earths with a mass of $3 \times 10^{-2}\, m_{\rm Jup}$ (equivalent to $\simeq 10$ Earth masses, in a sub-Neptune mass range). The RV amplitude of the later objects would be on the level of 2–3 m s^{-1}, relatively easily detectable with the present RV measurements accuracy. Also, in that case we set the system inclination $I = 60°$ to enhance the mutual gravitational influence between the planets and the test objects. In all experiments, the probe object interacts gravitationally with the three most massive planets.

To calculate the $\langle Y \rangle$ values for the synthetic systems, we integrated the N-body equations of motion and their variational equations with the GBS integrator (Hairer et al. 1993; Hairer & Wanner 1996) for $\simeq 10^5$ yr. Such an interval covers $\simeq 10^4$ orbital periods of outermost planet, which makes it possible to detect unstable motions associated with strongest two-body and three-body MMRs. This integration time is also consistent with the the typical characteristic time-scale required to achieve $\langle Y \rangle$ convergence for a stable configuration. The GBS integrator is the best choice in the case of collisional dynamics that is frequently expected in this setup.

4.1 Hypothetical asteroidal belts

The results for small-mass asteroids are illustrated in Fig. 13. Cartesian coordinates in the orbital plane of the system shown in the top panel are accompanied by plots for canonical elements of the test particles (bottom-right panel). We gathered $\simeq 10^6$ stable solutions with $|\langle Y \rangle - 2| < 0.007$ for this case. The probe particles are marked with different colours, depending on their dynamical status: brown dots are for objects involved in 1:1c MMR with the outermost planet HD 160691c; orange dots are for stable orbits between HD 160691b and HD 160691c, and blue dots are for the Kuiper belt-like zone beyond the outermost planet.

The edges of the debris disc formed in these regions are highly asymmetric. Also, their non-random distribution in the plane of the osculating elements (a_0, e_0) is shown in the bottom-right panel in Fig. 13. It was constructed based on the canonical elements determined in the Jacobi reference frame. The use of canonical elements is necessary to avoid the 'blurring' of the distribution that would otherwise occur with astrocentric elements. In this diagram, we marked the asteroids with the same colors as in the snapshot in the orbital plane, and some of the their lowest order MMRs with planet HD 160691c are labelled.

The results for the $\langle Y \rangle$-model may be confronted with dynamical maps computed in the (a_0, e_0)-plane for fixed orbital phases of the Vesta-like particles, shown in the left column in Fig. 13. The maps show the phase structure in three distance regions: between the innermost pair of planet HD 160691d and HD 160691e (the top panel), in the Main Belt zone (middle panel) and in the outer, Kuiper belt beyond the outermost planet HD 160691c (bottom panel). The resonant structure of the debris disks is also clear, especially in the bottom-left map. However, as expected, the Main Belt disc structures in the 2D dynamical maps are much more narrow than their representation in the $\langle Y \rangle$-model, due to fixed orbital phase of the test particles.

4.2 Earth-like planets and the habitable zone

Although we considered low-mass asteroids in this test, stable regions can potentially host larger planets as well, in the Earth mass range. As the mass of the probing objects increases, the regions may decrease in size, both in the coordinate and orbital element planes. This is illustrated in Fig. 14 for Earth-mass objects (the left column) and super-Earths (the right column), respectively. That case we should interpret in terms of a potential location of the small planets rather than a representation of a physical debris disc.

The distribution of Earth objects is very similar to the experiment for Vesta-type asteroids, as could be predicted from the similarity of this system to the restricted problem (with zero-mass asteroids). For more massive super-Earth 'asteroids' and the inclinations of the system $I = 60°$ the stable zones shrink considerably, but the overall
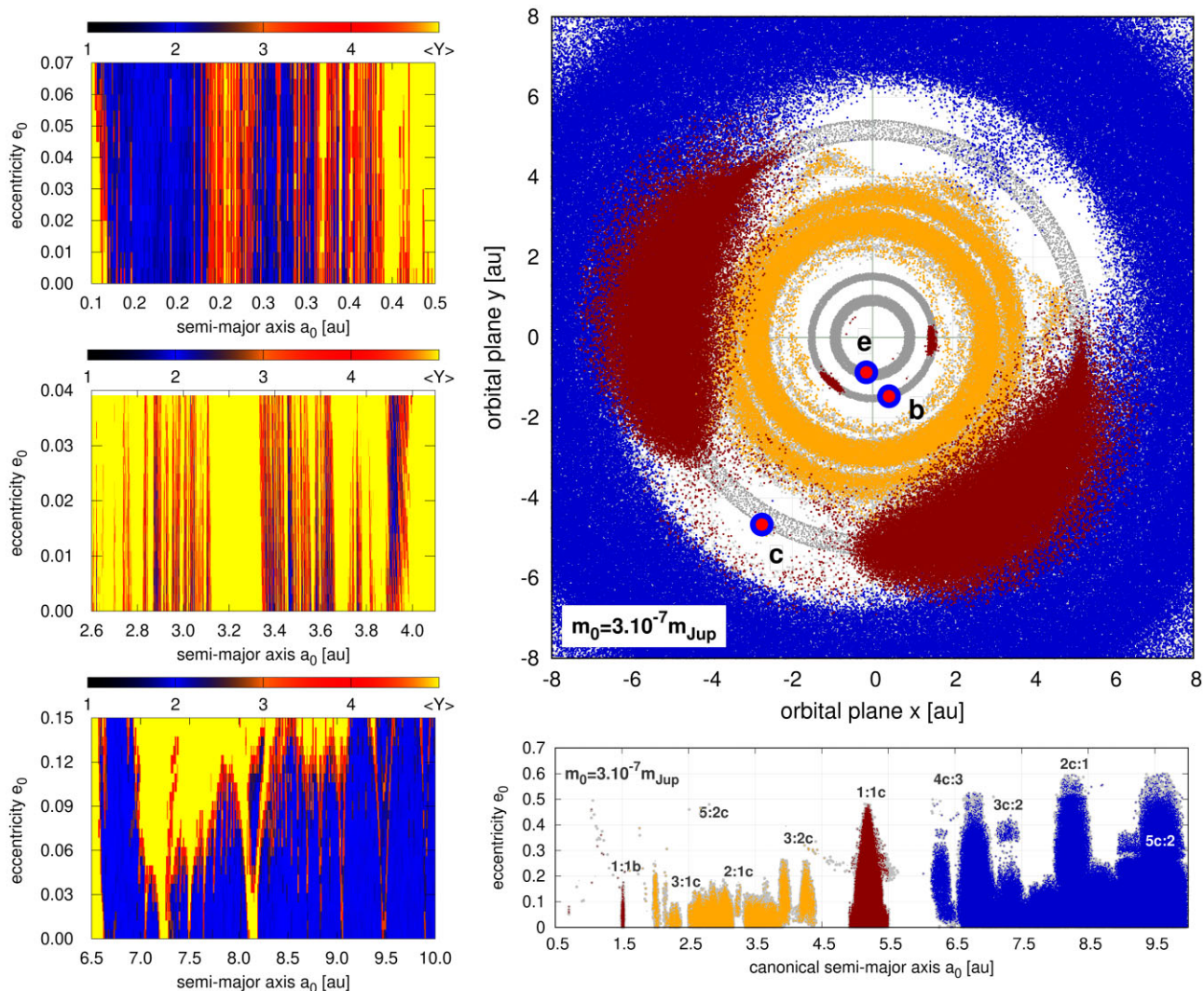
Figure 13. Left column: dynamical maps for a test particle (Vesta-like asteroid with the mass of $3 \times 10^{-7} m_{\text{Jup}}$) in three distinct regions between the planets. The MEGNO $\langle Y \rangle \sim 2$ indicates a regular (long-term stable) solution marked with black/dark blue colour, $\langle Y \rangle$ much larger than 2, up to $\gtrsim 5$ indicates a chaotic solution (yellow). The integration time of each initial condition is 10^5 yr ($\simeq 10^4 \times P_4$). Top-right panel: Debris disks in the HD 160691 system revealed by $\simeq 10^6$ stable orbits with $|\langle Y \rangle - 2| < 0.007$ gathered in the $\langle Y \rangle$-disk simulation. They are illustrated as a snapshot of astrocentric coordinates (x, y) at the initial epoch t_0. Colours of test particles injected with random elements, $a_0 \in [0.9, 10]$ au and $e_0 \in [0, 0.6]$) into the system of three outer planets, correspond to their dynamical status marked also in the panel with orbital elements, below. The initial positions of the planets are marked with filled circles. Grey rings illustrate their orbits integrated in a separate run for 0.2 Myr. Bottom-right panel: the orbital structure of hypothetical debris discs in the system, in terms of canonical Jacobi elements in the (a_0, e_0)-plane. Some two-body, lowest order MMRs with the planets are labelled, and stable orbits in their regions are marked with different colours, consistent with a snapshot of these stable solutions in the above panel.

discs structure is still preserved. We can conclude that the $\langle Y \rangle$-model scales for several orders of magnitude of the probe masses.

The results are therefore universal in the sense that we can predict the locations of e.g. Earth-like planets that are below the current detection limits. It turns out that such small planets could be found in the habitable zone, despite Rocinante and Quijote prevent stable orbits of terrestrial planets unless they are placed beyond roughly 2 au (see Fig. 14), or interior to 0.3–0.4 au.

Given the luminosity of μ Arae $L = 1.9 \, L_\odot$ and the spectral temperature $T = 5820$ K (Soriano & Vauclair 2010), the outer limiting distance roughly correspond to the orbit of Mars in the Solar system. Indeed, for an Earth-like planet, the inner radius of the runaway greenhouse effect is $r_{\text{min}} = 1.31$ au, the radius of maximum greenhouse effect $r_{\text{max}} = 2.30$ au, and the radius for early Mars zone $r_{\text{EM}} = 2.42$ au (Kopparapu et al. 2014, their habitable

zone calculator). Therefore, habitable Earth-like planets could be found in a small region of Lagrangian (Trojan) 1:1b orbits around HD 160691b as well on the inner edge of the Main Belt, up to the 3:1c MMR gap (see the elements distribution in Fig. 14).

5 CONCLUSIONS

The HD 160691 planetary system is one of the first detected multi-planet configurations with a mass-diverse planets, and it comprises of a warm Neptune, a Saturn-mass planet, and two massive Jupiter-mass objects. The precision RV data available in public archives, spanning at least 1.5 outermost periods, makes it already possible to tightly constrain the orbits and minimal masses of the planetary companions to $1\sigma \simeq 0.02 \, m_{\text{Jup}}$. Unfortunately, given a low accuracy of the *HST* astrometry reported in (Benedict et al. 2022), and insufficient
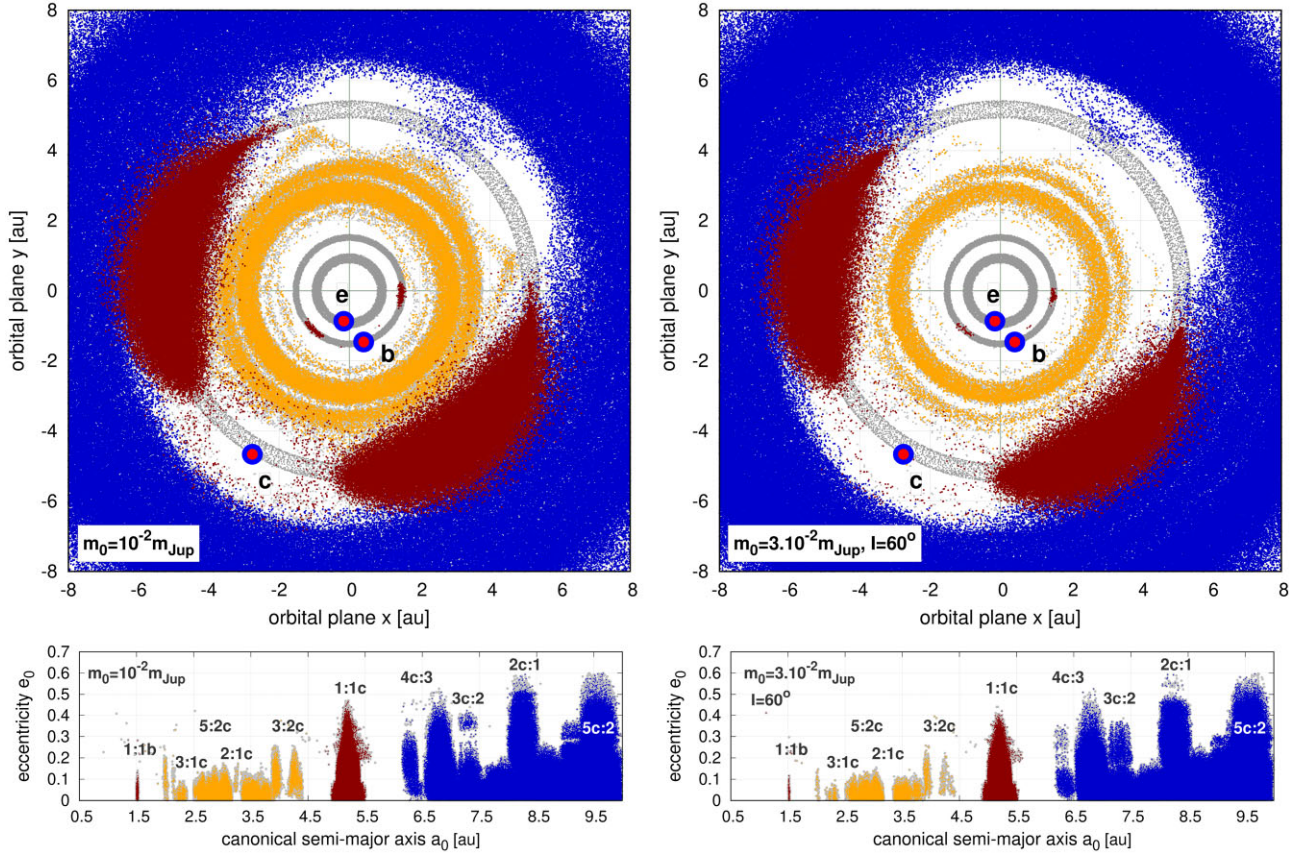
Figure 14. Stable orbits in the HD 160691 system revealed by $\simeq 10^6$ solutions with $|\langle Y \rangle - 2| < 0.007$ gathered in the $\langle Y \rangle$-disk simulation for a test planet masses m_0 injected into the system of three outer planets with random elements, $a_0 \in [0.9, 10]$ au and $e_0 \in [0, 0.6]$). They are illustrated as a snapshot of astrocentric coordinates (x, y) at the initial epoch t_0. Colours of the particles correspond to their dynamical status marked also in the panel with orbital elements, below. The initial positions of the planets are marked with filled circles. Grey rings illustrate their orbits integrated in a separate run for 0.2 Myr. The left column is for $m_0 = 0.01 m_{\mathrm{Jup}}$ (3 Earth-masses) and the right column is for $m_0 = 3 \times 10^{-2} m_{\mathrm{Jup}}$ (10 masses of Earth). The integration time with the GBS integrator of each initial condition is 10^5 yr ($\simeq 10^4 \times P_4$). Bottom panels are for the orbital structure of the stable orbits in terms of canonical Jacobi elements in the (a_0, e_0)-plane. Some two-body, lowest order MMRs with the planets are labelled, and stable orbits in their regions are marked with different colours, consistent with a snapshot of these stable solutions in the top panels.

detection limits (estimated here independently), we restricted the analysis to the RV data only.

We improved kinematic (Keplerian) models reported more than 15 yr ago (Goździewski et al. 2007; Pepe et al. 2007), as well as in the very recent paper by Benedict et al. (2022). Our Newtonian RV models of the HD 160691 system imply its long-term stable, Solar system-like orbital architecture. The planets revolve in low-eccentricity orbits determined with significantly reduced uncertainties $\simeq 0.01$ w.r.t. the prior literature, closely resembling the Earth–Mars–Jupiter sequence. Other orbital elements, and particularly the semimajor axes are bounded 0.02 au for the outermost planet, and to just 0.001–0.002 au for remaining inner massive companions. Limiting uncertainty of the outermost semimajor axis to $\simeq 27$ d means a qualitative improvement, compared to uncertainties of 700–1300 d reported in Goździewski et al. (2007) and Pepe et al. (2007).

Using the dynamical maps technique, we found that the nominal ICs cover regions in the phase space within several σ error bars that correspond to long-term stable evolution. The direct numerical integrations indicate stable orbital evolution of the best-fitting models for at least 6.7 Gyr (i.e. the lifetime of the star).

The present RV data do not make it possible to fully constrain the system inclination. However, it does not influence the stability in a wide range between $90°$ and $\simeq 20°$. In this range, coplanar systems remain in similarly wide and safe zones of stable motions, despite of planet masses enlarged a few times, in accord with the $m \sin I$ relation. Moreover, we found a close overlap of the dynamical stability with the best-fitting models in the sense that there is clear maximum of the posterior distribution for $\ln \mathcal{L}$ and a steep increase of the RMS at $I \simeq 20°$–$30°$. This means that all the masses would remain certainly below the brown dwarf mass range. It also proves that the analysed RV data bring information on the mutual interactions between the system components.

The meaningfully constrained orbits make it possible to globally investigate the global dynamical structure of the system. The inner pair of Saturn–Jupiter-mass planets is close to the 2e:1b MMR, but is significantly and systematically separated from this resonance. Similarly, the outer pair is close to the 6b:1c MMR but also is meaningfully far from it. This result may be important since it adds a new observational evidence on a near-resonant, well-characterized multiple system with Jovian-mass planets.

Multiple planetary systems, especially in the lower mass range detected by the Kepler mission, exhibit excess of planets close to

first order MMR (2:1 and 3:2), with the period ratio slightly higher than the resonant value (e.g. Petrovich et al. 2013; Delisle & Laskar 2014; Ramos et al. 2017; Marzari 2018, and references therein). There is a debate in the literature about the origin of this effect. It has recently been shown (Marzari 2018) that the presence of a massive circumbinary disc can significantly affect the resonant behaviour of a pair of planets, shifting the resonant position and reducing the size of the stability region. Dissipation of the disc may explain some exosystems that are close to the MMR but not trapped within it. If such mechanism was active in the μ Arae system, the current, near 2e:1b MMR for the inner pair could be a signature of a massive circumstellar disc in the past and its remnants in the form of asteroid belts at present. In this context, the evolution of the μ Arae system serves a particularly interesting scenario. The near-resonant pair is accompanied by a more distant high-mass companion, also near higher order 6c:1b MMR of the outer pair, which certainly enriches the dynamical setup.

The orbital architecture permits for the presence of massive debris disks, indeed, as they might survive between the planets. There is especially wide region between the outer pair, spanning the semimajor axes range of (1.5, 5.2) au; also there is such a vastly wide stable region beyond the outermost planet, starting at $\simeq$6.5 au and huge Trojan islands coorbital with the outermost planet. Simulations of these debris disks reveal their strongly resonant structure that is preserved in a wide range of probe masses, between Vesta-like asteroids and super-Earths with $\simeq$10 Earth masses. Te debris discs would be (obviously) strongly influenced by the MMRs with the Jovian planets. Their short-term MMR structure closely resembles the Main Belt and the Kuiper Belt in the Solar system.

Prospects to detect relatively massive, super-Earth–mass objects in the zone around 0.3–0.5 au or in other parts of the system, where stable orbits of are possible, are uncertain but unlikely. The semi-amplitude of their RV signals would be comparable with the intrinsic stellar jitter variability. We did not detect significant periods in the residuals of the RV models other than those identified with the known planets.

Because μ Arae has a fairly large parallax ($\simeq$65 mas), it may be an interesting and promising target for ALMA and other instruments to detect dust emissions, and set additional limits on the presence of small planets in outer parts of the system. In addition, the detection of debris disks, especially the outer one, can help better constrain the inclination of the system.

Monitoring the RV variability of the star still seems plausible, as it may permit to characterize the system even better, once the *Gaia* DR4 catalogue is released. Our simulation of the IAD measurements with the help of HTOF package (Brandt et al. 2021a) reveal that the two outer planets will be astrometrically detectable with very high S/N, provided the uncertainty of the IAD time series on the level of 0.1 mas. Moreover, we have shown that the mutual gravitational interactions can be detected in the RV data up to the middle of 2015. Additional precision RV observations might greatly help to break or reduce the $m \sin I$ degeneracy, and confirm or rule out the inclination of the system $I \simeq 20° - 30°$ indicated by our Bayesian MCMC sampling experiments.

Finally, the highly hierarchical configuration of μ Arae is a new test-bed for our new fast indicator REM (Panichi et al. 2017) that helps to analyse the structure of the phase space in terms of the most accurate, Newtonian representation of the data. Despite analytical approximations for the motion of the innermost planet may be constructed (Farago et al. 2009), the simple REM algorithm based on the canonical leap-frog scheme offers a sufficient numerical

efficiency to derive the dynamical maps through integrating the exact equations of motion of the whole system. It is also fully compatible with more CPU demanding MEGNO technique, especially for systems in regions of the the phase space which are filled with mostly stable solutions.

6 DATA AVAILABILITY

The Radial Velocity time series referenced in this paper as data set $\mathcal{D}_1$ are available in their source form, as published by Benedict et al. (2022) and as data sets $\mathcal{D}_2$ and $\mathcal{D}_3$ from (Trifonov et al. 2020, https://doi.org/10.1051/0004-6361/201936686), also https://github.com/3fon3fonov/HARPS_RVBank. All other data presented in Tables 1, 2, and Figures, underlying this article will be shared on reasonable request to the corresponding author.

REFERENCES

Agnew M. T., Maddison S. T., Horner J., 2018, MNRAS, 481, 4680
Baluev R. V., 2009, MNRAS, 393, 969
Barnes R., Greenberg R., 2007, ApJ, 665, L67
Benedict G. F., McArthur B. E., Nelan E. P., Wittenmyer R., Barnes R., Smotherman H., Horner J., 2022, AJ, 163, 295
Bonfanti A., Ortolani S., Piotto G., Nascimbeni V., 2015, A&A, 575, A18
Brandt G. M., Brandt T. D., Dupuy T. J., Michalik D., Marleau G.-D., 2021b, ApJ, 915, L16
Brandt G. M., Michalik D., Brandt T. D., Li Y., Dupuy T. J., Zeng Y., 2021a, AJ, 162, 230
Brandt T., 2021, ApJSS, 254, 42
Butler R. P. et al., 2006, ApJ, 646, 505
Butler R. P., Tinney C. G., Marcy G. W., Jones H. R. A., Penny A. J., Apps K., 2001, ApJ, 555, 410
Charbonneau P., 1995, ApJS, 101, 309
Cincotta P. M., Giordano C. M., Simó C., 2003, Phys. D Nonlinear Phenom., 182, 151
Claeskens G., Hjort N. L., 2008, Model Selection and Model Averaging. Cambridge Series in Statistical and Probabilistic Mathematics. Cambridge Univ. Press, Cambridge
Correia A. C. M., Bourrier V., Delisle J. B., 2020, A&A, 635, A37
Delisle J. B., Laskar J., 2014, A&A, 570, L7
Farago F., Laskar J., Couetdic J., 2009, Celest. Mech. Dyn. Astron., 104, 291
Foreman-Mackey D., Hogg D. W., Lang D., Goodman J., 2013, PASP, 125, 306
Gaia Collaboration, 2021, A&A, 649, A1
Goodman J., Weare J., 2010, Comm. Apl. Math. Comp. Sci., 1, 65
Goździewski K. et al., 2012, MNRAS, 425, 930
Goździewski K., Bois E., Maciejewski A., Kiseleva-Eggleton L., 2001, A&A, 378, 569
Goździewski K., Konacki M., Maciejewski A. J., 2003, ApJ, 594, 1019
Goździewski K., Konacki M., Maciejewski A. J., 2005, ApJ, 622, 1136
Goździewski K., Maciejewski A. J., Migaszewski C., 2007, ApJ, 657, 546
Goździewski K., Migaszewski C., 2018, ApJS, 238, 6
Guzzo M., 2005, Icarus, 174, 273

Hairer E., Nørsett S. P., Wanner G., 1993, Solving Ordinary Differential Equations I (2nd Revised. Ed.): Nonstiff Problems. Springer-Verlag, Berlin, Heidelberg

Hairer E., Wanner G., 1996, Solving Ordinary Differential Equations II. Stiff and Differential-Algebraic Problems, 2nd Revised Ed., Springer-Verlag, Berlin, Heidelberg, https://www.unige.ch/~hairer/

Jones H., Butler P., Marcy G., Tinney C., Penny A. J., McCarthy Ch., Carter B.D., 2002, MNRAS, 337, 1170

Kopparapu R. K., Ramirez R. M., SchottelKotte J., Kasting J. F., Domagal-Goldman S., Eymet V., 2014, ApJ, 787, L29

Laskar J., Petit A. C., 2017, A&A, 605, A72

Laskar J., Robutel P., 2001, Celest. Mech. Dyn. Astron., 80, 39

Laughlin G., Chambers J. E., 2001, ApJ, 551, L109

Lee M. H., Peale S. J., 2003, ApJ, 592, 1201

Marzari F., 2018, A&A, 611, A37

McCarthy C. et al., 2004, ApJ, 617, 575

Panichi F., Goździewski K., Turchetti G., 2017, MNRAS, 468, 469

Pepe F. et al., 2007, A&A, 462, 769

Petrovich C., Malhotra R., Tremaine S., 2013, ApJ, 770, 24

Ramos X. S., Charalambous C., Benítez-Llambay P., Beaugé C., 2017, A&A, 602, A101

Rein H., Spiegel D. S., 2015, MNRAS, 446, 1424

Ruciński M., Izzo D., Biscani F., 2010, Parallel Comput., 36, 555

Santos N. C. et al., 2004, A&A, 426, L19

Smart W. M., 1949, Text-Book on Spherical Astronomy. Cambridge Univ. Press, Cambridge

Soriano M., Vauclair S., 2010, A&A, 513, A49

Stalport M., Delisle J. B., Udry S., Matthews E. C., Bourrier V., Leleu A., 2022, A&A, 664, A53

Timpe M., Barnes R., Kopparapu R., Raymond S. N., Greenberg R., Gorelick N., 2013, AJ, 146, 63

Trifonov T., Tal-Or L., Zechmeister M., Kaminski A., Zucker S., Mazeh T., 2020, A&A, 636, A74

van Leeuwen F., 2007, Hipparcos, the New Reduction of the Raw Data, vol. 350, Astrophysics and Space Science Library, Springer Dordrecht

Wisdom J., 2006, AJ, 131, 2294

Wisdom J., 2018, MNRAS, 474, 3273

SUPPORTING INFORMATION

Supplementary data are available at *MNRAS* online.

Figure S1. 1D and 2D projections of the posterior probability distribution for orbital parameters of the innermost (left column) and the outermost (the right column) planet, respectively.

Figure S2. A fragment of the corner plot for posterior samples for the Keplerian model with an instrumental drift attributed to UCLES measurements.

Please note: Oxford University Press is not responsible for the content or functionality of any supporting materials supplied by the authors. Any queries (other than missing material) should be directed to the corresponding author for the article.

This paper has been typeset from a TEX/LATEX file prepared by the author.